Tectonophysics 788 (2020) 228502

Contents lists available at ScienceDirect

Tectonophysics

journal homepage: www.elsevier.com/locate/tecto

Zones of inelastic deformation around surface ruptures detected by magnetic fabrics

D. Elhanati[a,b,*], T. Levi[b], S. Marco[a], R. Weinberger[b]

[a] Department of Geophysics, Porter School of the Environment and Earth Sciences, Tel-Aviv University, Tel-Aviv 69978, Israel
[b] Geological Survey of Israel, 32 Yesha'ayahu Leibowitz St., Jerusalem, 9692100, Israel

ARTICLE INFO

Keywords:
Magnetic fabrics
AMS
Faults
Paleoseismology
Dead sea fault

ABSTRACT

Characterizing the inelastic strain field around co-seismic faults is a key to understanding earthquake rupture processes. We aim to detect zones of inelastic deformation around surface ruptures, using Anisotropy of Magnetic Susceptibility (AMS) analyses. To characterize the paleo-seismic setting we measured 29 normal faults, which cut the late Pleistocene lacustrine Lisan Formation and were associated with shallow (< ~12 km) earthquakes at the margins of the Dead Sea Basin. In order to define the geometry of those zones around a representative fault, 220 specimens were sampled in a 2D grid and analyzed by studying the room temperature AMS axes and parameters using spatial IDW (inverse distance weighting) interpolation on a cross section around the fault plane. To separate the total magnetic susceptibility of the Lisan sediments into diamagnetic, paramagnetic and ferromagnetic susceptibilities, we applied the low temperature AMS (LT-AMS) and Anhysteretic Remanent Magnetization (AARM) methods. The structural measurements demonstrate that the co-seismic faulting in the Dead Sea Basin, triggered mainly by *E*-W extension. The results show that the paramagnetic phase is dominant in both the aragonite-rich and the detritus-rich layers. The zones of inelastic deformation are distributed asymmetrically about the fault plane, with affinity to the observed displacement profile and in agreement with dynamic propagation models that suggest that the rupture propagated towards the surface. The discontinuous distribution of deformation around the fault plane is the result of both the faults single event propagation style and fault plane asperities. These results demonstrate a novel application of AMS analysis for defining the geometry of the inelastic strain field surrounding co-seismic faults, and improving fault propagation models dealing with the inelastic off-fault response.

1. Introduction

During an earthquake, unrecoverable inelastic deformation together with elastic deformation develop next to co-seismic (i.e., dynamic) faults (Ma and Andrews, 2010; Shearer, 2009). This envelope of deformed volume around the faults, known as a "damage zone", has received much attention over the years, as it is a key component in earthquakes and faulting processes (Ma and Andrews, 2010; Rice et al., 2005). Once the yield stress of the host rock is exceeded, the region around the fault deforms inelastically, leading to stress relaxation, dissipation of energy and formation of the associated damage zone (Madhur et al., 2014). Hence, characterizing zones of inelastic deformation is critical for understanding earthquake-related faulting. Despite the importance in determining the principal axes, size and spatial distribution of the inelastic strain field around the dynamic fault, these three variables cannot always be defined for paleo-earthquakes. This is due to scarcity of visible kinematic indicators complicated by the very fine-grained fault gouge and changes in the style of deformation with depth. In order to overcome these difficulties, we use the Anisotropy of Magnetic Susceptibility (AMS) analysis, which indicates the preferred orientation of the different minerals and grains in the rocks. In many cases this alignment is the result of the inelastic strain stored in the rock, and can serve as a microscopic kinematic indicator useful for defining the strain field in the deformed rocks. The AMS analysis is a useful proxy for characterizing strain directions as demonstrated in many structural studies of sedimentary and igneous rocks (e.g., Borradaile and Jackson, 2010; Levi et al., 2014; Tarling and Hrouda, 1993a; Weinberger et al., 2017 and references therein). Relative to other methods used for detection of rock fabrics (e.g., X-ray diffraction; Fusseis et al., 2014; Li et al., 2017; Martínez-Martínez et al., 2016), AMS is a fast and robust method, which results in an average magnetic fabric consisting of the contribution of all different minerals

* Corresponding author at: Department of Geophysics, Porter School of the Environment and Earth Sciences, Tel-Aviv University, Tel-Aviv 69978, Israel.
E-mail address: dan.elhanati@gmail.com (D. Elhanati).

https://doi.org/10.1016/j.tecto.2020.228502
Received 22 December 2019; Received in revised form 22 May 2020; Accepted 26 May 2020
Available online 30 May 2020
0040-1951/

and grains in the rock (Borradaile, 1988). Since the three principal AMS axes are commonly coaxial with the directions of the three principal strain axes, analyzing the magnetic fabrics near co-seismic faults may reveal the components of the inelastic strain field that has developed during fault propagation.

In this study, we analyze the AMS axes and parameters using Geographical Information System (GIS) to define the zones of inelastic deformation around surface ruptures, cross-cutting the late Pleistocene Lake Lisan sediments within the seismically active Dead Sea Basin. The geometric reconstruction of these zones allows us to better understand their formation in association with dynamic fault propagation near the surface.

2. Geologic setting

The study area is located in Masada Plain, next to the western margin of the Dead Sea pull-apart basin. In this area, the Masada Fault Zone consists of dozens of NNW to NNE-striking *syn*-depositional normal faults, cross-cutting the Lisan Formation (Marco and Agnon, 2005). The Masada Fault Zone is a part of the Dead Sea Fault system (DSF), which is an active plate-bounding zone that stretches for about 1000 km, from the northern part of the Red Sea Rift to the East Anatolian fault zone in Turkey, and forms the boundary between the Arabian and African (Sinai) plates (Fig. 1a). The trace of the DSF along its southern segment in Sinai and Israel is characterized by a series of en-echelon elongated depressions, extending from the Gulf of Elat (Aqaba) Basin in the south and through the Arava Basin, Dead Sea Basin, Jordan and the Hula Basins in the north (Fig. 1b, Garfunkel et al., 1981).

The Dead Sea Basin is a 150 km long, 15–20 km wide pull-apart structure that was formed between the left-stepping Arava and Jericho master faults. The western margin of the Dead Sea pull-apart basin is composed of a ~ N-S belt of zig-zag faults striking between NNE and NNW and dipping either eastward or westward. These faults are mainly, with minor dextral or sinistral components, striking NNE and NNW respectively (Braun et al., 2015; Sagy et al., 2003). They represent *E*-W extension and N-S contraction and do not show significant lateral displacement, which seems to be limited to the faults further to the east.

The rocks exposed in Masada Plain belong to the late Pleistocene Lisan Formation, which comprises a ~ 40 m thick lacustrine sediments consisting mostly of horizontal laminae of authigenic aragonite and gypsum layers alternating with fine detritus layers (Begin et al., 1974). The aragonite precipitated chemically from the upper surface of Lake Lisan (the precursor of the Dead Sea), whereas the fine detritus, which contains mainly clay minerals, was carried by annual floods. The lacustrine sediments are currently widely exposed within the DSB (Fig. 1b) due to significant shrinkage of Lake Lisan at beginning of the Holocene. The U−Th age of the Lisan Formation is between ~70,000 and 15,000 years B·P (Haase-Schramm et al., 2004).

Past earthquakes triggered coseismic deformation, including *syn*-depositional faults (Marco and Agnon, 1995), injection clastic dikes (Levi et al., 2011; Levi et al., 2006a); horizontal slip along bedding planes (Weinberger et al., 2016) and subaqueous slump folds within the Lisan Formation (Alsop et al., 2017). Paleoseismic records from the Dead Sea Basin based on breccia layers reveal numerous M > 5.5–6 earthquake events during the last 70,000 years (Enzel et al., 2000; Ken-Tor et al., 2001; Marco et al., 1996), as well as several M > 7 earthquake events (Begin et al., 2005, and references therein). The strongest recorded event in the Dead Sea Basin was the M = 6.2 earthquake of 11 July 1927; its source mechanism was of a left-lateral motion (Ben-Menahem et al., 1976; Shapira et al., 1993).

3. Anisotropy of magnetic susceptibility (AMS)

3.1. General

Magnetic susceptibility [*K*] is a dimensionless second-order tensor, which indicates how much a material will be magnetized ($\vec{M}$) in response to an applied magnetic field ($\vec{H}$). The tensor is described by three principal axes, $K_1(K_{max})$, $K_2(K_{int})$ and $K_3(K_{min})$, which correspond to the maximum, intermediate and minimum eigenvalues magnitudes, $k_1(k_{max})$, $k_2(k_{int})$ and $k_3(k_{min})$, respectively. The AMS is describable by a magnitude ellipsoid, somewhat similar in concept to the finite strain ellipsoid with principal susceptibilities as its axes (e.g., Borradaile and Jackson, 2010). Different parameters depend upon the axial relationship of the susceptibility ellipsoid (Jelínek, 1981): the mean susceptibility ($k_m = \frac{k_1 + k_2 + k_3}{3}$); anisotropy degree ($P = \frac{k_1}{k_3}$); AMS shape factor ($T = \frac{2n - n_1 - n_3}{n_1 - n_3}$), where n_1, n_2 and n_3 are the natural logarithms of the principal susceptibilities and $n = \frac{n_1 + n_2 + n_3}{3}$; $T = \ - 1$ represents a prolate ellipsoid, $T = 0$ represents a neutral ellipsoid and $T = 1$ represents an oblate ellipsoid; magnetic lineation ($L = \frac{k_1}{k_2}$) and magnetic foliation ($F = \frac{k_2}{k_3}$). The *T* and *L* parameters, are both indicative of the rock's deformation history (Borradaile and Jackson, 2010; Levi et al., 2019), and therefore can be used to detect deformation-induced magnetic fabrics.

3.2. Magnetic fabrics in geologic settings

Both the AMS and the strain are represented as second-rank tensors and magnitude ellipsoids, which led to several attempts of correlation between the two (e.g. Borradaile, 1991; Borradaile, 1987; Casas-Sainz et al., 2018; Hirt et al., 2000; Hrouda, 1993; Soto et al., 2009, and references therein). In many cases of deformed environments, fair to good correlation was found between the directions of the principal strain axes and the directions of the principal AMS axes (Borradaile, 1991; Borradaile, 1988; Borradaile, 1987; Borradaile and Henry, 1997; Issachar et al., 2015; Levi et al., 2014; Levi and Weinberger, 2011; Mamtani and Sengupta, 2009; Oliva-Urcia et al., 2013; Pares et al., 1999; Soto et al., 2007; Tarling and Hrouda, 1993a). In extensional basins, the K_1 axes are either subparallel to the dip directions (Mattei et al., 1999; Mattei et al., 1997) or correspond to the maximum stretching direction (Cifelli et al., 2005). Prominent AMS fabrics in sedimentary rocks have also been shown to develop under contractional strain (Borradaile, 1988; García-Lasanta et al., 2013; Oliva-Urcia et al., 2013), during horizontal slip along bedding planes (Weinberger et al., 2016), and due to movement of mass transport deposits (Weinberger et al., 2017).

Lineations and foliations of magnetic fabrics may form as a result of sedimentary processes, such as deposition and compaction (Hrouda, 1982; Taira, 1989; Tarling and Hrouda, 1993a) and transport of clastics (e.g. Levi et al., 2006a; Rees, 1971; Rees and Woodall, 1975). Under earthquake-triggered instability, the sediments may be transported and associated with various types of deformed structures (e.g., slumps and brecciated layers; Marco and Agnon, 2005; Beck, 2009). The inelastic strain field at the propagating dynamic fault tip may facilitate re-arrangement of particles, obliterating the deposition fabrics and forming deformation fabrics (Levi et al., 2014). Different minerals and grains may have a different physical response to deformation, resulting in a net magnetic fabric composed of different sub-fabrics (Borradaile and Jackson, 2004). Under sedimentary still environments, the particles settle scattered on the bedding planes (e.g., Rees, 1971; Rees and Woodall, 1975), and the AMS fabric is characterized by well-grouped vertical K_3 axes perpendicular to the bedding plane and scattered K_1 and K_2 axes, which lie on the bedding plane (hereafter, “deposition fabric”). Under deformation environments, for example in an extensional regime (Soto et al., 2007), the remote (i.e., tectonic) or local strain field aligns the particles such that K_3, K_2 and K_1 axes are well grouped and coaxial with the maximum (ε_1), intermediate (ε_2) and minimum (ε_3) shortening axes, respectively (hereafter, “deformation fabric”; for more details see Levi et al., 2014).

The deformation fabric of the Lisan Formation was previously

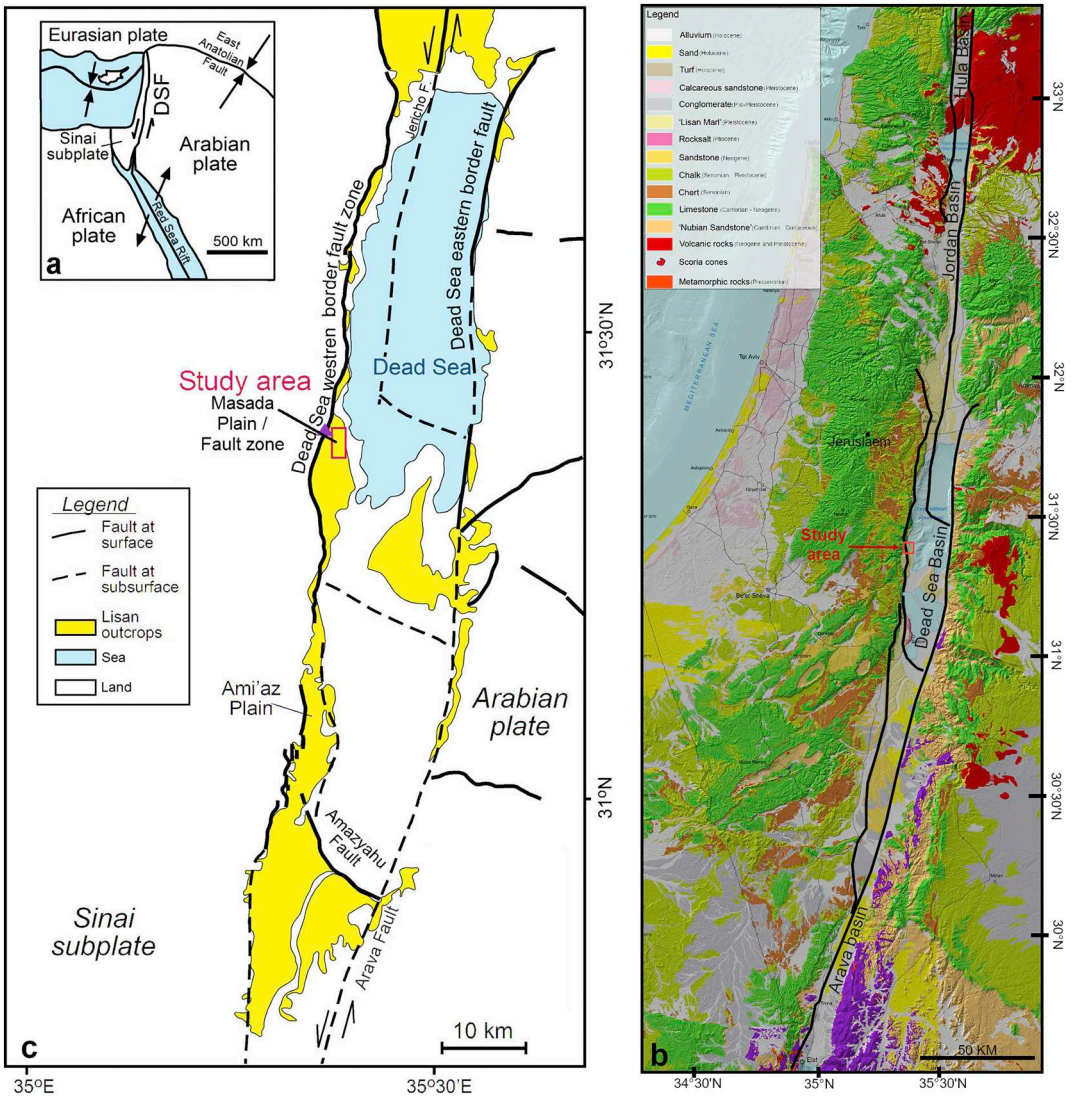

Fig. 1. a) Plate tectonic configuration along the Dead Sea Fault system (DSF). b) Geological map along the DSF after Sneh et al. (1998); Fault segments are marked by black lines after Sneh and Weinberger (2014). c) Regional setting of the Dead Sea Basin and outcrops of the lacustrine Lisan Formation, after Sneh and Weinberger (2014). Masada Plain is marked by a red rectangle. Solid lines – main faults at the surface; dashed lines – main faults at the sub-surface; purple triangle – location of Masada, a world heritage site.

studied near three co-seismic normal faults in the Masada Fault Zone, which formed surface ruptures at the bottom of Lake Lisan (Levi et al., 2014). The study shows that the deformation fabrics were developed up to tens of centimeters from the fault planes, whereas the deposition fabrics prevail meters away from these planes. The results also demonstrate that the deformation-driven magnetic fabrics and the associated inelastic strain fields are compatible with co-seismic dynamic faulting. The present study analyzes the fabrics in a 2D grid around a representative fault, which allows studying the full spatial extent of deformation surrounding the fault in decimeter resolution.

3.3. Magnetic properties of the Lisan Formation

The white laminae of the Lisan Formation consist mainly of diamagnetic aragonite, while the brownish-green detritus laminae carry weak remanent magnetization in titanomagnetite, magnetite and greigite grains (Levi et al., 2006b; Ron et al., 2006). A specimen composed of mostly aragonite (hereafter, "aragonite-rich layer") show a weak paramagnetic susceptibility, while a specimen consisting of mostly detritus (hereafter, "detritus-rich layer") have a higher paramagnetic susceptibility. Specifically, the larger titanomagnetite grains (pseudo-single domain and multi domain) were identified as the main ferromagnetic minerals in the detrital layers. The hysteresis curve indicates that the titanomagnetite grains are pseudo-single domain (PSD) to strong multi-domain (MD) size (Ron et al., 2006). Temperature-dependence susceptibility curves also indicate the presence of titanomagnetite as well as magnetite (Levi et al., 2006a).

4. Methods

4.1. Structural measurements and sampling strategy

Structural data, including fault-plane orientation and throw, were collected from 29 faults in Masada Plain. Kinematic indicators such as slickensides and lineations are generally absence in the soft rock along the studied fault planes. We therefore assume that the slip motion is parallel to the dip direction, based on previous works, which studies displaces markers such as clastic dikes (Jacoby et al., 2015; Marco et al., 1996; Marco and Agnon, 2005). The *P* (Pressure) and *T* (Tension) axes and focal-plane solutions were calculated using FaultKin 5.2.3 (Allmendinger et al., 2011; Cardozo and Allmendinger, 2013; Marrett and Allmendinger, 1990). The different structural characteristics were

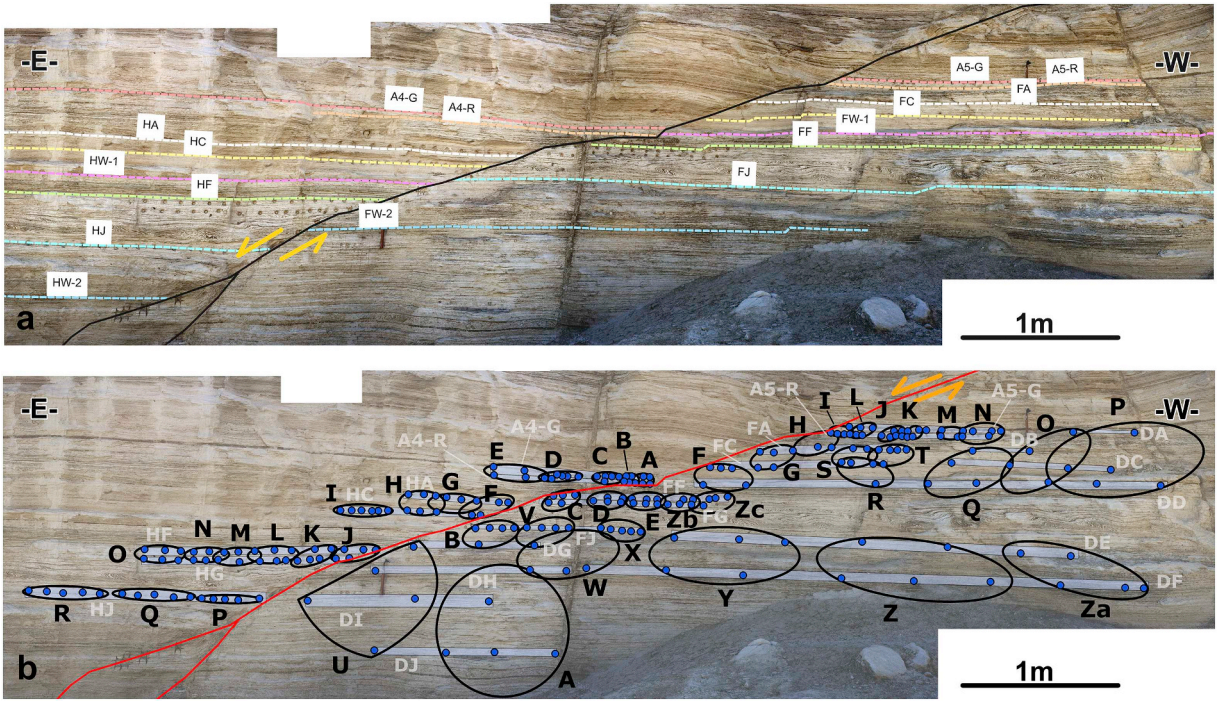

Fig. 2. a) Cross section of the studied fault. The trace of the fault is marked by a solid black line. Dashed colour lines mark pairs of layers (i.e., markers) on both sides of the fault. b) Sampling scheme around the studied fault. Blue dots mark the extracted specimens, taken along horizontal levels marked and labeled in light grey. Black circles mark the groups used for spatial analyses of magnetic fabric (labeled in black); some specimens are shared between the groups to satisfy statistical requirements. A4 and A5 (G and R) were taken as representative specimens for the study of magnetic fabric in aragonite-rich and detritus-rich layers. (For interpretation of the references to colour in this figure legend, the reader is referred to the web version of this article.)

plotted on map using GIS, and their spatial distribution was analyzed. In two representative faults (#3_2 and #1, Supplementary Data, item #1) the displacement (D) along the fault length (L) in a cross-sectional view was measured in order to construct a displacement profile, D/L.

The zones of inelastic deformation were studied around a representative fault (#3_2), which was extensively sampled for magnetic fabric analysis. The studied fault was chosen due to the following advantages: 1) Compared to the other faults, it is characterized by a high maximum displacement value (D_{max} = ~2.35 m); 2) The non-deformed horizontal layers near the fault are easily correlated from both sides of the fault and can be used to construct the D/L profile (Figs. 2a and 3) The fault is accessible for sampling.

In total, 220 oriented specimens were collected from seven layers, observed in both the hanging wall and the footwall and some layers sampled only from the footwall, using 25 × 20 mm (height x diameter) Perspex (Polymethyl methacrylate) cylinders, which have negligible diamagnetic susceptibility. The specimens along horizontal and distinct laminae were sampled up to ~2 m away from the fault plane at ~5 cm increments, and further up to ~5 m away from the fault plane, at ~0.5 m increments (Fig. 2b). To test the effect of the mineral composition in the Lisan layers on the magnetic fabrics, the specimens were sampled from both aragonite-rich and detritus-rich layers. Based on Levi et al. (2014), the content of the $CaCO_3$ in the aragonite-rich layers in average is ~60%, while in the detritus-rich layers it is significantly lower than ~50%.

4.2. AMS and rock magnetism

Room-temperature AMS (RT-AMS), Low-temperature AMS (LT-AMS) and Anisotropy of Anhysteretic Remanent Magnetization (AARM) were measured with *Agico KLY-4S Kappabridge*, *AMU-1A* magnetizer, *LDA-3A* demagnetizer and a *JR-6A* spinner magnetometer at the magnetic fabric laboratory of the Geological Survey of Israel. RT-AMS measurements were performed on all 220 specimens with a 300 A/m induced magnetic field. The room temperature was kept stable at 24° to avoid measuring errors due to instrument sensitivity. LT-AMS measurements were performed on selected specimens in order to investigate which magnetic phases are the main carriers of the AMS. Performing LT-AMS measurements is similar to AMS measurements, and generally requires cooling down the specimen and subsequently conducting the regular AMS measurement. We have followed the protocols developed by Soto et al. (2014) and Issachar et al. (2016). The latter introduce an LSR (i.e., molded liquid silicone rubber, commonly used in cookware) sleeve to protect the instrument coil and reduce measuring errors. The application of this method for the Lisan specimens encased in Perspex cylinders proved technically difficult, as many specimens were destroyed by the rapid cooling and heating induced by exposure to liquid nitrogen. In order to measure the magnetic fabric of the ferromagnetic minerals, the AARM method was applied in which the specimen is subjected to a strong (100 mT) alternating magnetic field, which removes magnetization, and at the same time to a weak (50 μT) direct magnetic field, resulting in the net magnetization of the specimen parallel to the direction of the direct field. The remanent magnetization vector was then measured. AARM measurements were performed on selected specimens with the purpose of comparing the results of both methods (and LT-AMS).

To test the possibility that the mineral compositions control the types of magnetic fabric and their spatial distribution around the fault plane, we compare the AMS and magnetic mineralogy data of representative detritus-rich and aragonite-rich layers from both sides of the fault (See Fig. 2b: A4-G, A4-R, A5-G and A5-R).

For the spatial analyses, we interpolate the AMS data in a cross section around the fault by three different methods: 1) Calculating the acute angle difference that forms between the K_1 axes and the strike or dip direction of the fault (hereafter, Ψ parameter, see next paragraph), and interpolating around the fault; 2) grouping of the deposition and the deformation fabrics around the fault (See Figs. 2b and 3) Interpolating the values of T-L and P parameters around the fault.

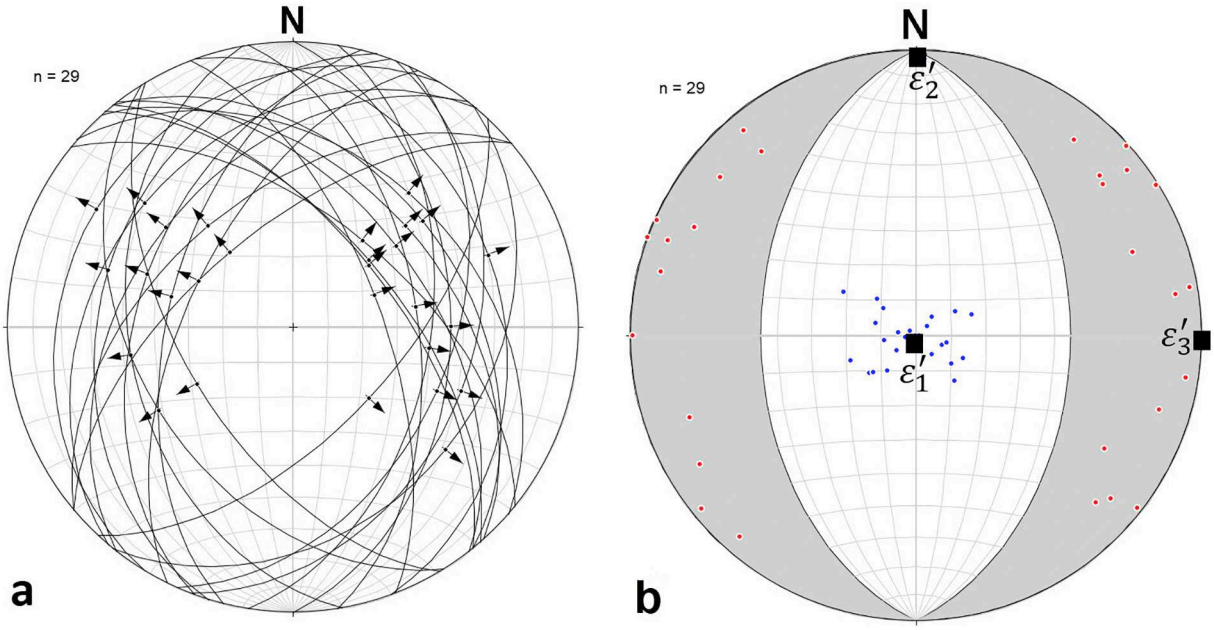

Fig. 3. a) Stereographic projection of fault planes. Arrows mark the fault slip directions. b) A moment-tensor solution for the fault population displaying a north-south striking normal faulting (Pressure/Tension axes, blue/red dots, respectively). ε_1', ε_2', and ε_3' are the infinitesimal maximum, intermediate and minimum principal strain axes, respectively. (For interpretation of the references to colour in this figure legend, the reader is referred to the web version of this article.)

Deformation fabrics related to faulting might be associated with either K_1 or K_2 axes parallel to the strike of the nearby fault (Levi et al., 2014). The K_1 axes may be parallel either to the strike or to the dip direction (i.e., the K_2 axes are parallel to the strike). The Ψ variable combines the two options by representing the minimal angle difference that forms between the K_1 axes and the strike or the dip direction of the fault. Therefore, we use Ψ to test the affinity of the deformation fabric to the faulting – in which a low Ψ implies that there is a high affinity between the deformation fabric and the fault.

The data are also presented on T-ln(L) plot, used to reveal the kinematics and dynamics of a wide variety of seismites in soft sediments. On this plot, high T (> 0.5) and low L values (< 1.005) are classified as deposition fabrics, while low T (< 0.5) and high L (> 1.005) values are classified as deformation fabrics (Levi et al., 2018). The magnitudes and directions of the AMS axes, as well as the 95% confidence angles and mean tensor values were calculated using the software package *Anisoft 42*, which uses the statistical methods of Jelínek (Jelínek, 1981).

To characterize the ferromagnetic minerals of the Lisan layers near the fault, temperature dependent susceptibility measurements and Isothermal Remanent Magnetization (IRM) were preformed using *KLY-4S* Kappabridge with a *CS3* furnace and *ASC model IM10–30* Impulse Magnetizer, at the paleomagnetic laboratory of the Institute of Earth Sciences, the Hebrew University of Jerusalem. The AF Demagnetization and the magnetization measurements were conducted using the *LDA-3A* demagnetizer and *JR-6A* spinner magnetometer, respectively.

4.3. Susceptibility phase separation

The separation of the total magnetic susceptibility into diamagnetic, paramagnetic and ferromagnetic susceptibilities, was carried out by combining the measurements of RT-AMS, LT-AMS and AARM (e.g. Issachar et al., 2016; Soto et al., 2014, and references therein).

The mean susceptibility measured in room temperature is defined as the sum of diamagnetic, paramagnetic and ferromagnetic respective mean susceptibility contributions:

$$k_m^{RT} = k_{md} + k_{mp} + k_{mf} \quad (1)$$

The mean susceptibility measured in low temperature is defined as:

$$k_m^{LT} = k_{md} + \alpha \bullet k_{mp} + k_{mf} \quad (2)$$

where α is the ratio between room temperature and the low temperature (3.2 at a room temperature of 273 K and a low temperature of 85 K – the temperature of liquid nitrogen).

By subtracting (1) from (2) we obtain the paramagnetic mean susceptibility - at room temperature:

$$k_{mp} = \frac{k_m^{LT} - k_m^{RT}}{\alpha - 1} \quad (3)$$

It should be noted that Eq. (3) assumes that the mean susceptibilities of the diamagnetic and ferromagnetic phases are temperature independent. In the case of the ferromagnetic phase, the mean susceptibility may change at low temperatures, namely due to Verwey transition in magnetite-titanomagnetite, or Morin transition in hematite (Morin, 1950; Verwey, 1939). Nonetheless, where rocks are characterized by a relatively high ratio of paramagnetic to ferromagnetic content, it is expected that the susceptibility change at low temperature be controlled by the paramagnetic phase. As the susceptibility of pure aragonite is -15×10^{-6} SI (Tarling and Hrouda, 1993b), the diamagnetic mean susceptibility can be estimated using the content of aragonite in the aragonite-rich and detritus-rich layers (see 4.1), yielding a diamagnetic mean susceptibility of -10×10^{-6} SI and -6×10^{-6} SI, respectively. After obtaining both k_{mp} (using Eq. (3)) and k_{md}, k_{mf} is calculated using (1).

5. Results

5.1. Structural data

Table 1 (Supplementary Data, item #1) summarizes the structural measurements of each fault, including the fault-plane orientation and maximum throw. The stereographic projection of the fault planes (Fig. 3a) shows two main sets of faults: 1) Sixteen faults dipping to the east (synthetic to the major Dead Sea west margin fault) and 2) Thirteen faults dipping to the west (antithetic to this fault). The dip and dip direction of the synthetic faults (in average) are 50° and 104°, respectively, whereas the dip and dip direction of the antithetic faults (in average) are 46° and 254°, respectively. The derived fault-plane

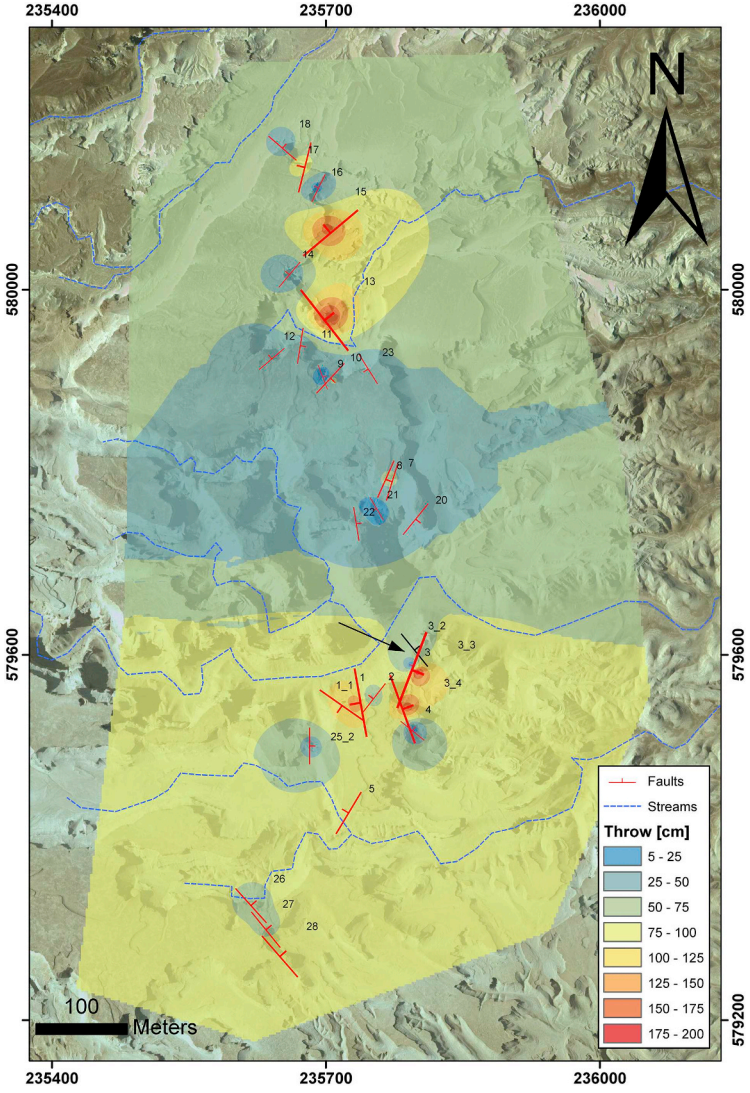

Fig. 4. Interpolation analysis of the fault's throws in the study area (n = 29). The faults are marked with red symbols. The size and direction of the symbol corresponds to the fault's throw and dip direction, respectively. The studied fault is marked with a black arrow. Dashed blue lines mark the main streams in the study area. (For interpretation of the references to colour in this figure legend, the reader is referred to the web version of this article.)

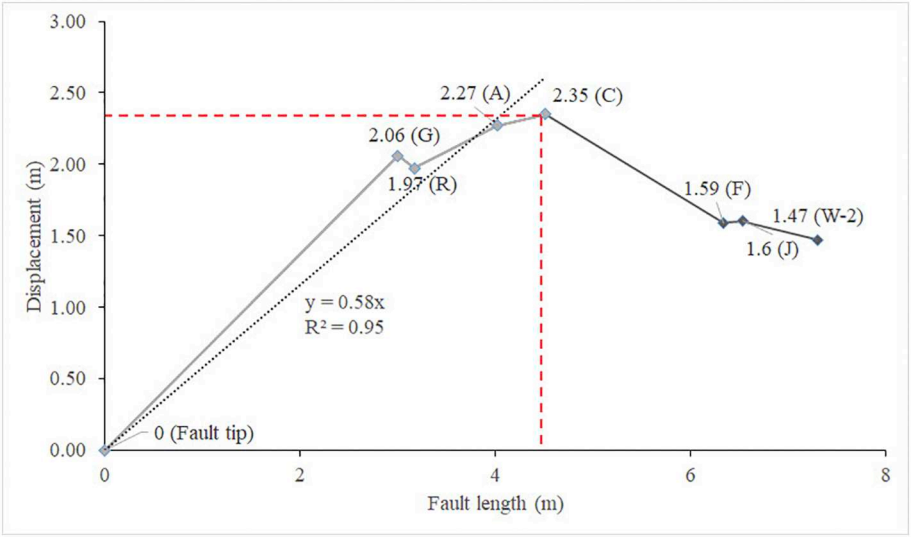

Fig. 5. Displacement/length profile of the studied fault (based on markers presented in Fig. 2a). The maximum displacement along the fault length is indicated by the red dashed lines. Dashed black line marks the linear correlation fitted from the maximum displacement to the fault's tip (displacement = 0). (For interpretation of the references to colour in this figure legend, the reader is referred to the web version of this article.)

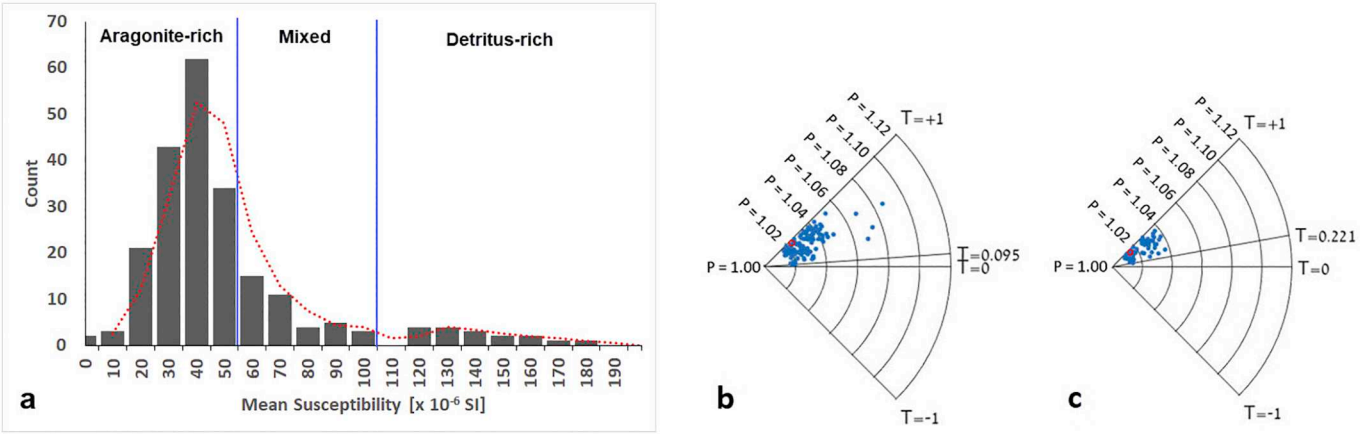

Fig. 6. a) Histogram of mean susceptibilities of all specimens (N = 220). The moving average curve is marked with a red dashed line. b) Polar *P/T* plot of the aragonite-rich layers (*T* values range between 0.095 and 1; *P* values range between 1.02 and 1.08). c) Polar *P/T* plots of the detritus-rich layers (*T* values range between 0.221 and 1; *P* values range between 1.005 and 1.04). Reference values from Ami'az Plain (Levi et al., 2018) are marked with red dots. (For interpretation of the references to colour in this figure legend, the reader is referred to the web version of this article.)

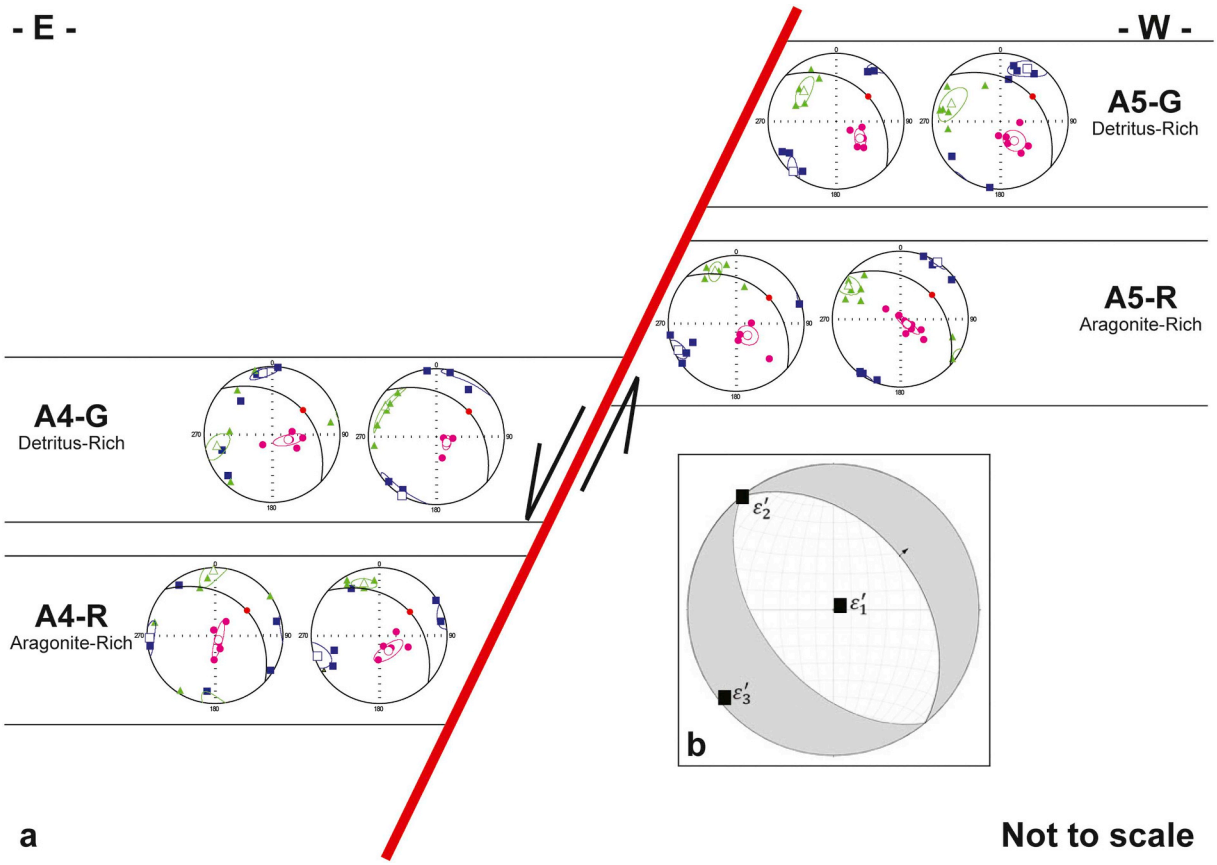

Fig. 7. a) Deformation fabrics identified in two distinct layers on both sides of the fault. A great circle and a red dot mark the fault plane and dip direction, respectively. Blue square, green triangle and purple circle mark the K_1, K_2 and K_3 AMS axes, respectively (See Supplementary Data, item #3 for AMS data table). b) A moment-tensor solution calculated for the studied fault. Arrow marks the dip-slip direction. ε_1', ε_2', and ε_3' are the infinitesimal maximum, intermediate and minimum principal strain axes, respectively. (For interpretation of the references to colour in this figure legend, the reader is referred to the web version of this article.)

solution shows an average N-S striking normal mechanism, with maximum vertical shortening (ε_1') and maximum *E*-W horizontal extension (ε_3', Fig. 3b). The maximum throw along the fault planes ranges between 5 and 189 cm, with an average value of 68 cm (Supplementary Data, item #1). Based on the interpolation map of the throw of the normal faults (Fig. 4), two areas of high maximum throw (1.5–2 m) are identified in the study area: one in the northern part and the other in the southern part of the study area.

Fault #1 and fault #3_2 are located near the southern contour of maximum throw. In fault #1, 17 pairs of layers (hereafter, "markers") were identified in the footwall and hanging wall whereas in fault #3_2 eight pairs of layers were identified in the footwall and hanging wall (Fig. 2a). The *D/L* of Fault #1 is characterized by semi-trapezoid shape (Marco and Agnon, 2005) with maximum displacement of 2.5 m

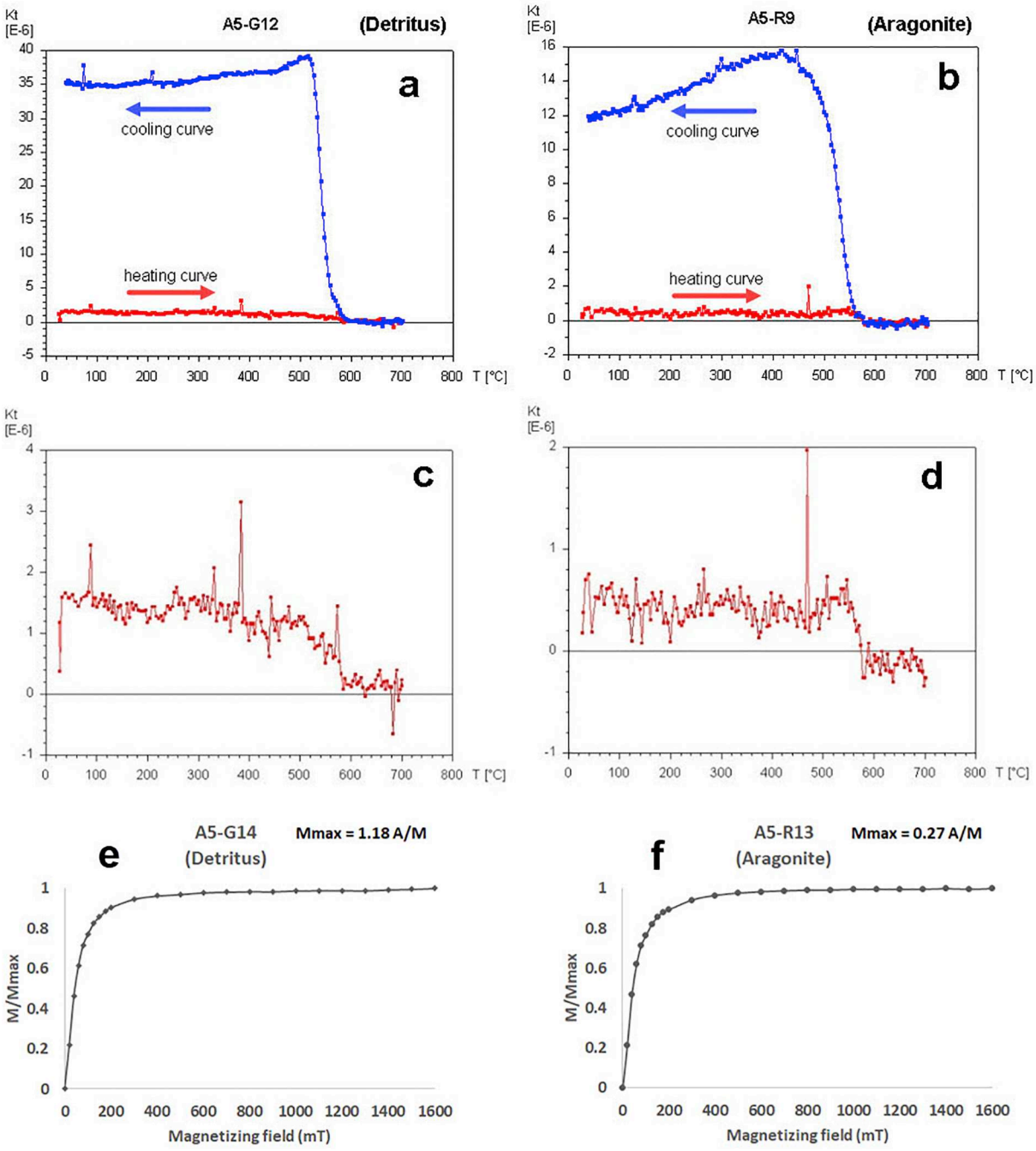

Fig. 8. Representative thermomagnetic curve for: **a**) detritus-rich layer and b) aragonite-rich layer**.** c) and d) are enlarged heating curves for the detritus-rich and aragonite-rich layers, respectively. The steep gradient of the susceptibility around 600 °C in both curves is attributed to magnetite/titanomagnetite. e) and f) IRM curves of the detritus-rich and aragonite-rich layers, respectively. Saturation values and the associated magnetic fields are similar for both specimens, and are typical of magnetite. The detritus-rich layers (e) show much higher maximum saturation values than the aragonite-rich layer values (f).

(Supplementary Data, item #2), while the displacement profile of Fault #3_2 is characterized by triangle (cone) shape (Muraoka and Kamata, 1983) with maximum displacement of 2.35 m (Fig. 5). In both faults the displacement decreases steeply along the fault towards the surface until reaching zero displacement.

5.2. Effect of mineral composition on magnetic fabrics

The mean susceptibility values of the Lisan specimens are between 5 and 186 $\times$ 10^{-6} SI with an average value of 55 $\times$ 10^{-6} SI (Fig. 6a). Most of the specimens of the aragonite-rich layers have lower susceptibility values ($<$ 50 $\times$ 10^{-6} SI) than those of the detritus-rich layers with P values ranging from 1.02 to 1.08 (Fig. 6b). Specimens of detritus-rich layers have higher susceptibility values ($>$ 100 $\times$ 10^{-6} SI) with P values ranging from 1.005 to 1.04 (Fig. 6c). Specimens containing a mixed composition of aragonite and detritus have susceptibility values ranging from 50 to 100 $\times$ 10^{-6} SI (Fig. 6a).

Fig. 7a shows the magnetic fabrics of two pairs of distinct layers located on both sides of the fault. Two are aragonite-rich layers (labeled R), and the other two are detritus-rich layers (labeled G). In all four layers, deformation fabrics are identified, in which the three AMS axes are well grouped. In the footwall specimens, the K_1, K_2 and K_3 axes are compatible with the fault plane solution (ε_3', ε_2' and ε_1' respectively, Fig. 7b). In the hanging wall, a similar behavior is observed for the

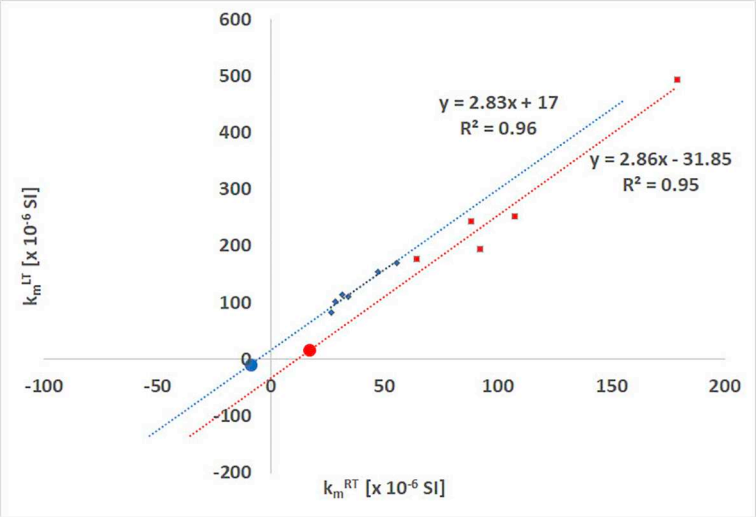

Fig. 9. k_m^{RT}/ k_m^{LT} plot for aragonite-rich (blue) and detritus-rich (red) layers. The intercept where $k_m^{RT} = k_m^{LT}$ is marked by filled dots. (For interpretation of the references to colour in this figure legend, the reader is referred to the web version of this article.)

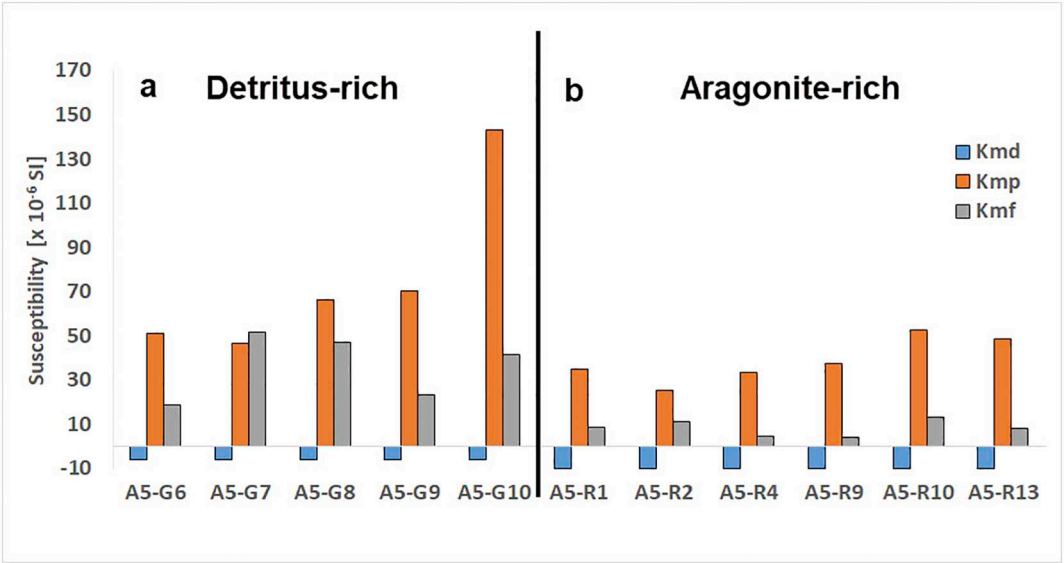

Fig. 10. Contribution of the ferromagnetic (K_{mf}), paramagnetic (K_{mp}) and diamagnetic (K_{md}) susceptibilities to the total susceptibility in (a) detritus-rich layers and (b) aragonite-rich layers, using Eqs. (1) and (3) (see text).

specimens close to the fault plane, while in the specimens located away from the fault plane the directions of the AMS axes are more diverse. The adjacent aragonite-rich and detritus-rich layers have similar magnetic fabrics as seen in the stereograms of Fig. 7.

5.3. Magnetic mineralogy and phase separation

The thermomagnetic curves (Fig. 8a,b) of the aragonite-rich and detritus-rich layers show that the dominant magnetic carrier of all specimens is magnetite, characteristic of the Lisan Formation (Levi et al., 2006b; Marco et al., 1998). The heating and cooling curves of both materials decreases gently around 580 °C, attributed to the Curie temperature of magnetite (Butler, 1998). The higher susceptibility values of the cooling curves can be attributed to formation of new magnetite under high temperatures (Hrouda, 1994). The thermomagnetic curve of the detritus-rich specimen is characterized by a higher susceptibility value (40×10^{-6} SI) than the aragonite-rich specimen (16×10^{-6} SI), due to the high content of ferromagnetic minerals in the former.

The IRM acquisition curves (Fig. 8e,f) shows saturation around 300 mT (Butler, 1998), which is indicative of magnetite grains. While the average maximum magnetization of detritus-rich layers is 1.035 A/M, the aragonite-rich layers are 0.2225 A/M (average). This large difference implies that the detritus-rich layer has a high concentration of ferromagnetic minerals, consistent with their high mean susceptibility value (Fig. 6a).

The k_m^{LT}/ k_m^{RT} plot of aragonite-rich and detritus-rich layers shows a high linear correlation ($R^2 = 0.95$, Fig. 9), which indicates mostly constant diamagnetic and ferromagnetic contents and varied paramagnetic contents (Issachar et al., 2018). The aragonite-rich and detritus-rich layers have similar k_m^{LT}/k_m^{RT} slopes (2.84 and 2.87 for aragonite and detritus, respectively), which is close to the expected value (~3.2) for pure paramagnetic samples (Issachar et al., 2016). The intercept where $k_m^{RT} = k_m^{LT}$, is -9.3×10^{-6} SI for the aragonite-rich layer and 17.01×10^{-6} SI for the detritus-rich layer. These two intercepts indicate the predicted sum of mean susceptibility of the diamagnetic and ferromagnetic phases in the aragonite-rich and detritus-rich layers, respectively (i.e., $k_m = k_{md+}k_{mf}$). Based on the procedure

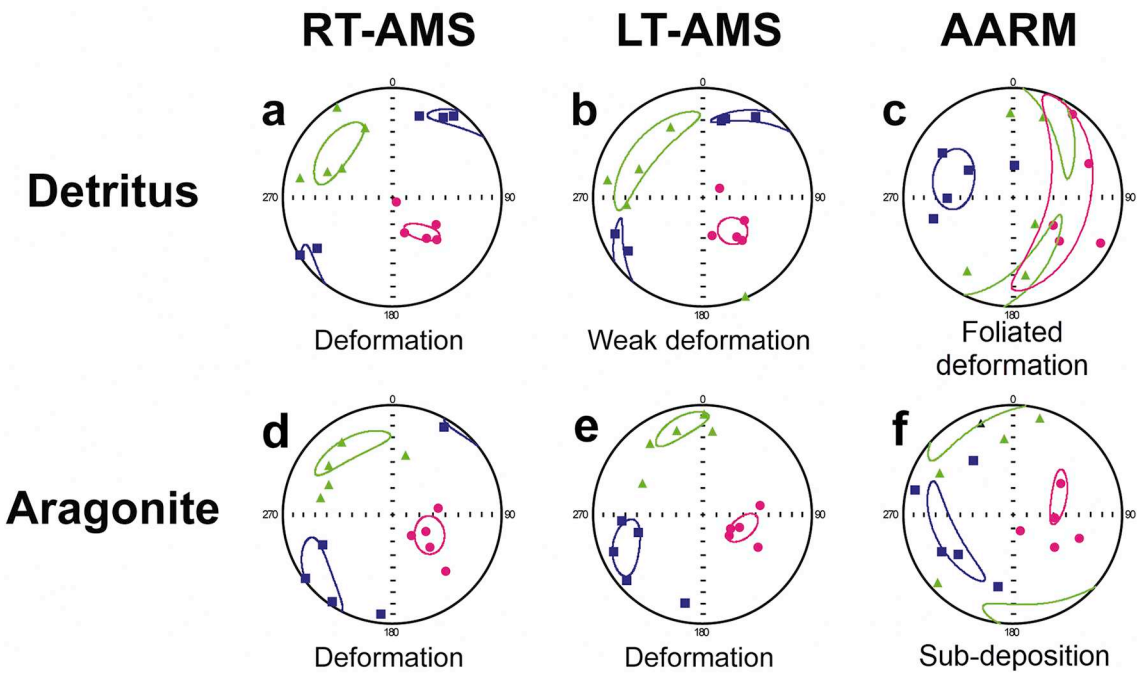

Fig. 11. Magnetic fabrics of detritus-rich and aragonite-rich layers measured by RT-AMS (a and d), LT-AMS (b and e) and AARM (c and f) methods. Blue square, green triangle and purple circle mark the K_1, K_2 and K_3 axes, respectively. (For interpretation of the references to colour in this figure legend, the reader is referred to the web version of this article.)

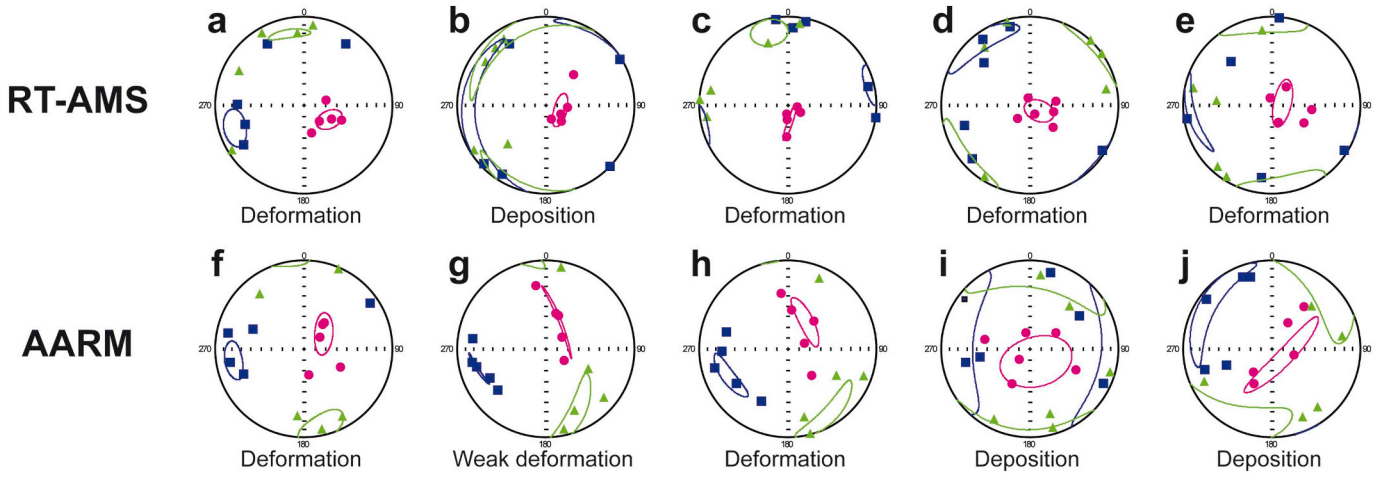

Fig. 12. RT-AMS fabrics (a-e) compared with AARM fabrics (f-j) of two distinct layers on both sides of the fault (Fig. 7a; A4-G, A5-G, A4-R and A5-R). Blue square, green triangle and purple circle mark the K_1, K_2 and K_3 axes, respectively. (For interpretation of the references to colour in this figure legend, the reader is referred to the web version of this article.)

described in Section 4.3, Fig. 10 shows the contribution of each magnetic phase to the total mean susceptibilities measured in the aragonite-rich and detritus-rich layers. Both types of layers show a weak diamagnetic contribution to the total mean susceptibility, compared to the paramagnetic and ferromagnetic phases. In the detritus-rich layers, this finding is more dominant as the ferromagnetic and paramagnetic contributions (up to ~97%) are much larger than that of the diamagnetic contribution phase (up to ~8%). In the aragonite-rich layers, the paramagnetic phase is the main contributor (up to 70%) to the total mean susceptibility for all specimens. In the detritus-rich layers, the ferromagnetic phase could equally contribute to the total mean susceptibility as the paramagnetic phase.

The comparison of the RT-AMS, LT-AMS and AARM fabrics of representative specimens (aragonite-rich and detritus-rich layers) shows similar deformation fabrics for the RT-AMS and LT-AMS, in which the K_1, K_2 and K_3 axes are well grouped and have the same mean directions (Fig. 11). In both methods the confidence ellipses are somewhat similar. The AARM measurements of the same representative specimens shows a foliated deformed fabric for the detritus-rich layer (Fig. 11c), whereas in the aragonite-rich layer a sub-deposition fabric is seen (Fig. 11f).

The comparison of the RT-AMS and AARM measurements of representative specimens shows three different cases: (1) deformation fabrics for both RT-AMS and AARM analyses (Fig. 12, a and c versus f and h), (2) deposition and deformation fabrics for RT-AMS and AARM analyses, respectively (Fig. 12, b versus g), and (3) deformation and deposition fabrics for RT-AMS and AARM analyses, respectively (Fig. 12, d and e versus i and j).

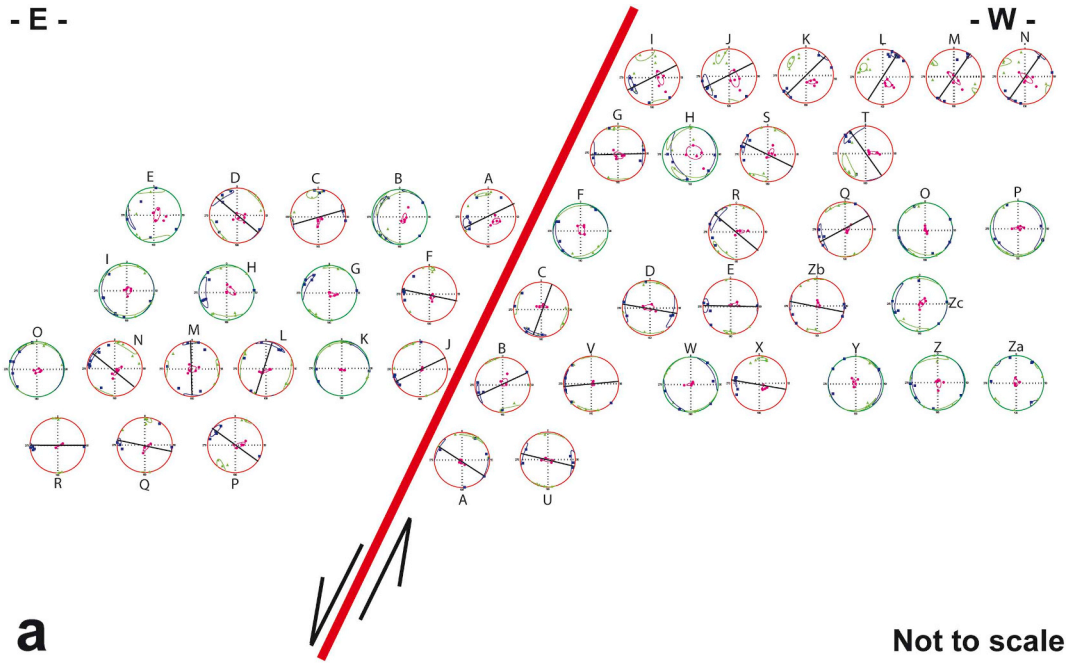

Fig. 13. a) lower-hemisphere, equal-area projections of AMS principal axes and the 95% confidence ellipses (Jelínek, 1981) around the studied fault. Deformation fabrics are marked by a red circle, while deposition fabrics are marked by a green circle. K_1 axes of deformation fabrics are marked by a black line (See Supplementary Data, item #4 for AMS data table). b) AMS axes analysis around the fault. Red and green zones mark the deformation and deposition fabrics, respectively. c) Interpolation of the Ψ variable around the fault. Red and green zones have high and low affinity to the fault, respectively. d) Interpolation of the *T*-*L* values around the fault. Red and green zones mark areas of high *L*/low *T* and high *T*/low *L*, respectively. The point of maximum displacement along the fault is marked by a yellow diamond. (For interpretation of the references to colour in this figure legend, the reader is referred to the web version of this article.)

5.4. Spatial distribution of magnetic fabrics

Fig. 13a and Table 3 (Supplementary Data, item #4) shows the magnetic fabrics in the area surrounding the fault: deposition fabrics (16 stereograms marked by green circle) and deformation fabrics (31 stereograms marked by red circle). The two types of fabrics do not seem to appear in specific distances from the fault plane, but rather in a patch-like pattern. While in some areas, the deformation fabrics display K_1 axes, which are parallel to the fault plane solution ε_3' shortening axis, the remaining deformation fabrics display varied directions of K_1 axes.

Based on the AMS axes analysis using GIS, four main deformation zones are identified as follows (Fig. 13b): Two zones are located asymmetrically at the fault edges, where the displacement values are the lowest, and two zones are located in the center of the fault trace, where the displacement values are the highest. In the footwall and hanging wall, the main deformation zones are located up to 2.5 m and 1.5 m away from the fault plane, respectively. Fig. 13c shows the distribution of the Ψ variable around the studied fault. Similar to the AMS axes analysis, the Ψ analysis shows the patch-like pattern, in which the AMS axes are arranged in an asymmetrical geometry around the fault. While the Ψ map shows many areas with affinity to the fault, the four aforementioned deformation zones have distinctively low Ψ values, implying high affinity to the faulting process.

Based on the analysis of the *T*-*L* values, three deformation zones are identified (Fig. 13d), where two zones are located asymmetrically at the fault edges similar to the map of the AMS axes analysis (Fig. 13b). In this method, the main deformation zone in the footwall is located up to 2 m away from the fault plane, while in the hanging wall the main deformation zone is located up to 1 m away from the fault plane. The contouring of the *P* parameter shows that the area with the highest *P* values is located mainly in the upper section of the footwall (Supplementary Data, item #5).

Fig. 14 shows the *T*/ln(*L*) plot of specimens that are presented in Fig. 13a. Based on the fabric types, two main groups are obtained: deposition fabrics (group A), with *T* values ranging from $T = 0.79$ up to $T = 0.95$ and *L* values ranging from $L = 1.001$ up to $L = 1.03$, and deformation fabrics (group B), with *T* values ranging from $T = 0.49$ up to $T = 0.91$ and *L* values ranging from $L = 1.001$ up to $L = 1.06$ (see also Levi et al., 2018).

6. Discussion

6.1. Co-seismic faulting in Masada Plain

The normal faults in Masada Plain are an expression of moderate to strong (see below) earthquakes that occurred during the late Pleistocene along the western margin of the Dead Sea Basin (Marco and Agnon, 1995). The focal plane solution of 29 normal faults (Supplementary Data, item #1) represents earthquake events, which are characterized by *E*-W extension (Fig. 3b). These findings are in agreement with studies carried out in the Dead Sea Basin (Braun et al., 2015; Marco and Agnon, 1995; Sagy et al., 2003) and in the other basins (Issachar et al., 2018; Issachar et al., 2015; Levi et al., 2019) located along the southern sector of the DSF. These studies show that during the Plio-Pleistocene the left-lateral motion was accompanied by an extensional component, normal to the trace of the DSF. Furthermore, these findings are in agreement with fault measurements in the Wadi Darga fan-delta, located about 20 km north of the study area, which were attributed to Holocene earthquake events (Eyal et al., 2002).

The observations show that the normal faults in the study area propagated close to the surface or even ruptured the surface. Considering that the maximum throw close to the surface was up to 2 m (Fig. 4), it can be assumed that the earthquakes were strong enough to rupture the bottom of Lake Lisan. The interpolation of throw in the study area has shown two local maxima regions: in the northern and southern parts of the study area (Fig. 4). Two possible alternatives may explain these findings: (1) The local maximum throw regions represent two distinct fault segments, which may further merge downwards in the sub-surface, and (2) The two local maximum throw areas represent two

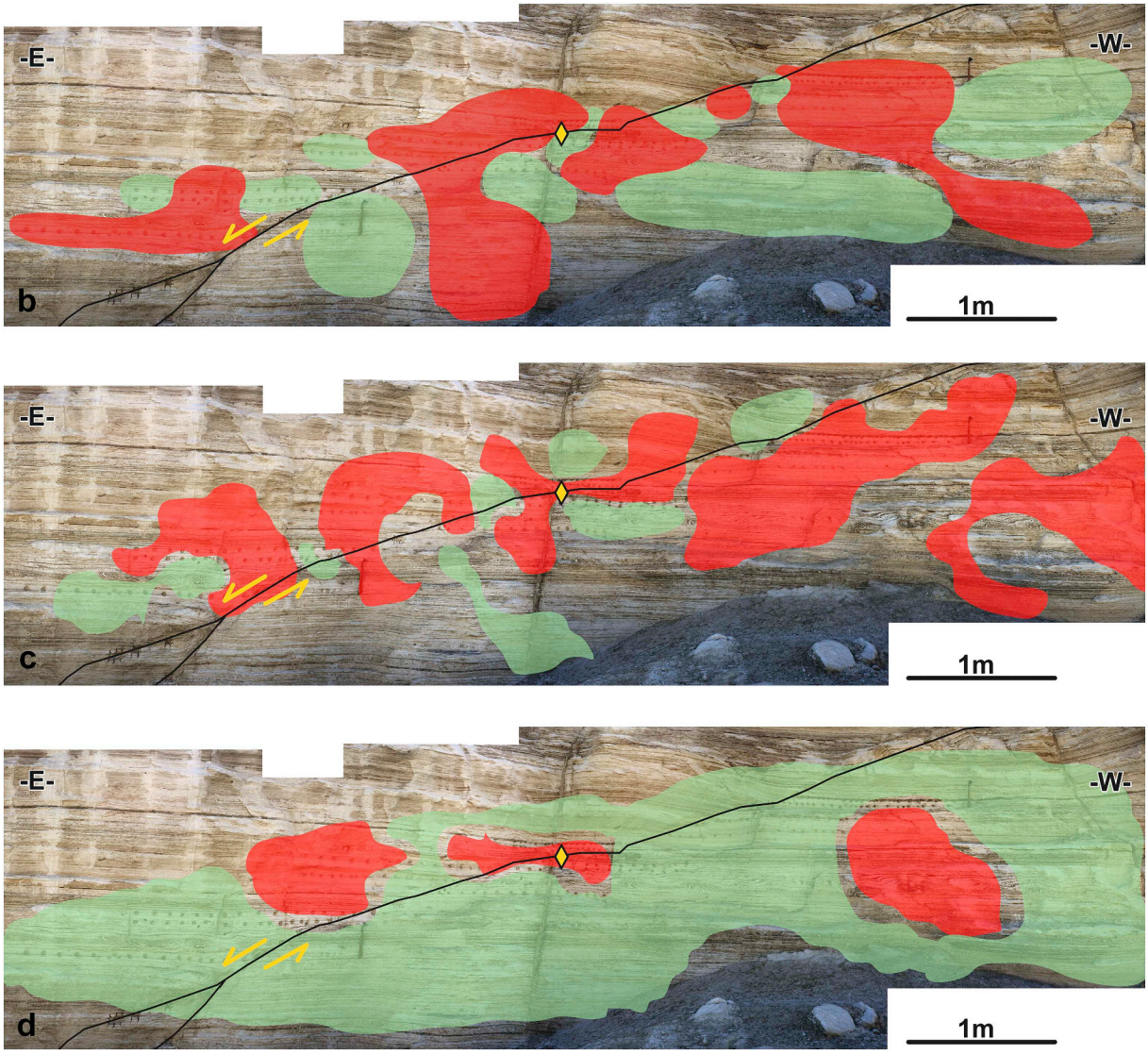

Fig. 13. (*continued*)

different earthquake events that were focused in different parts along a single sub-surface master fault. In agreement with the first alternative, seismic reflection profiles show that in the sub-surface close to the study area the DSF system is characterized by a normal (negative) "flower structure" where in Masada Fault Zone the fault traces are extending ~250 m below the surface (Agnon et al., 2006) and probably merged further at depth (Fig. 15).

According to Marco and Agnon (1995) the observed surface ruptures at the bottom of Lake Lisan in the study area were formed during three to five earthquake events with magnitudes of M > 5.5. This suggestion has been corroborated later by measuring the seismites around faults (Marco et al., 1996), and by measuring the cumulative slip along co-seismic faults (Marco and Agnon, 2005). The results show that Fault #1 that exhibits three slip events, characterized by a semi-trapezoid shape of D/L with D_{max} = 2. 5 m (Supplementary Data, item #2). On the other hand, Fault #3_2 is characterized by a triangle (cone) shape of D/L with D_{max} = 2.35 m (Fig. 5). Bearing in mind that the D/L profile is more likely to appear as triangle-shape in a single event (Kim and Sanderson, 2005), it is suggested that the studied fault (#3_2) propagated during a single event. In that case, the maximum displacement of 2.35 m (i.e., dip separation) suggests a minimum earthquake magnitude of M = ~6.5 (Wells and Coppersmith, 1994). Hence, it is likely that the exposed faults in Masada Plain represent the upward fault propagation of the Dead Sea western margin fault towards the surface under E-W extension, coaxially with extensional stress. We suggest that some of the faults, including the studied fault could have developed during moderate (M = ~6–6.5) earthquake events (Fig. 15).

6.2. Zones of inelastic deformation around surface ruptures

The aragonite-rich and detritus-rich layers are differentiated by their magnetic susceptibility values, temperature dependent susceptibility, and IRM analyses (Figs. 6, 8). However, they have similar values (in average) of AMS parameters (Fig. 6b,c), share the same types of magnetic fabrics and Ψ values near and away from the studied fault (Fig. 7, see #6.3 below). In addition, the aragonite-rich and detritus-rich layers share the same deformation fabrics that are compatible with the fault-plane solution (Fig. 7b). Notably, the analysis of the $T/\ln(L)$ plot (Fig. 14) greatly strengthens the separation of the magnetic fabrics into deposition and deformation fabrics (Fig. 13a). Hence, it appears that the deformation fabrics indicate the spatial extent of the inelastic deformation formed by the co-seismic faults with no dependency on the type of lithology (either aragonite-rich or detritus-rich layers).

Static strain accumulates near the fault plane or tip during the arrest of fault propagation, usually due to long-term steady plate motions. If the deformation fabrics were formed under such conditions, a

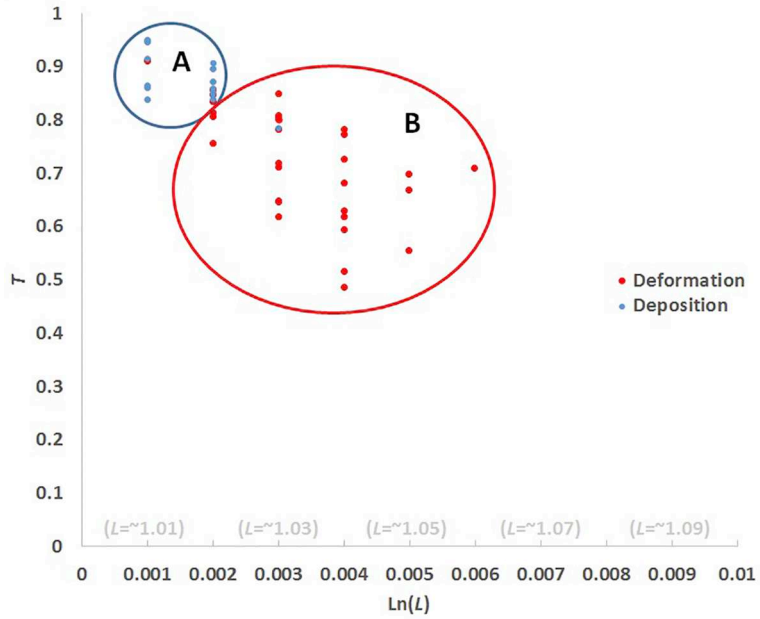

Fig. 14. T/ln(L) plot. Specimens of deposition (blue ellipse, group A) and deformation (red ellipse, group B) fabrics are marked by blue and red dots, respectively. (For interpretation of the references to colour in this figure legend, the reader is referred to the web version of this article.)

symmetrical distribution of deformation fabrics around the fault would be expected (Faulkner et al., 2010), in disagreement with the present observations (Fig. 13). Moreover, it is questionable whether the very low strain magnitudes expected near the surface would be enough to change deposition fabrics into deformation fabrics, considering also the properties of the soft Lisan sediment (i.e. wet), and its low cohesion.

The analyses of the magnetic fabrics around the representative fault shows five main findings that can be further explained by models of dynamic rupture propagation: 1) The AMS axes of the deformation fabrics vary from one place to another with regard to the fault's dip direction. While some of the K_1 or K_2 axes are sub-parallel to the dip of the fault, the directions of other K_1 or K_2 are varied. This indicates that the inelastic strain creates distinct deformation fabrics, but it does not necessarily cause the K_1 or K_2 axes to align with the dip direction; 2) Two zones are located asymmetrically at the fault edges, where the displacement values are the lowest, and one (Fig. 13d) or two zones are located at the center of the exposed fault trace, where the displacement values are the highest (Fig. 13b). This indicates that the zones of inelastic deformation becomes wider in the hanging wall and the footwall as the distance increases from the maximum displacement point (Fig. 13); 3) Among the deformation zones, along the trace of the fault (e.g., Fig. 2a), there are several areas (green polygons in Fig. 13) that have not undergone a significant inelastic deformation; 4) The widest zone of inelastic deformation is diagnosed in the upper section of the footwall, which is also characterized by higher degree pf anisotropy (P) values and seven AMS stereograms which are compatible with the fault-plane solution (Fig. 7b); and 5) The maximum width of the inelastic deformation zone (W_m = 2.5 m) in the footwall is similar to the maximum displacement (D_m = 2.35 m) measured in the representative fault (Fig. 5).

Ma and Andrews (2010) present 3D models of dynamic rupture propagation under conditions of low confining pressure. These models show that the inelastic strain field is changeable around the propagated ruptrues, in agreement with the present results, which show that the directions of AMS axes may vary significantly in the deformation zones (finding #1). In dynamic fracture propagation, the size of the damage zone and its geometry depend mainly on the ruptrue propagation velocity (Rice et al., 2005). In this mode of formation, the width of the inelastic zone (W), could be much narrower than that formed by the quasi-static propagation, and could be asymmetric around the faults (Ben-Zion and Shi, 2005; Faulkner et al., 2011; Rice et al., 2005). The extent of the inelastic deformation increases with the propagation distance (either bilaterally or unilaterally) from the point of maximum displacement (finding #2). For a non-planar dynamic rupture, the asymmetric zone of inelastic deformation shows discontinuities within it, where deformation has not been accumulated (finding #3). This phenomenon occurs due to the formation of stress perturbations caused by fault roughness which impacts the rupture propagation. The heterogeneities affect the slip distribution, cause rapid accelerations and decelerations of the rupture front, and affect the occurrence of plastic strain (Madhur et al., 2014, Fig. 4d).

In the present study, the range of W/D_{total} values (roughly between 0.1 up to 1.4), the variations of the K_1 or K_2 axes (finding #1), the asymmetrical geometry of the inelastic strain field (finding #2), the formation of patches of inelastic deformation (finding #3) and the similarity between W_m and D_m (finding #5), all strongly support the development of the inelastic deformation during a single event of dynamic fault propagation. If there had been multiple propagation events, we would expect a continuous inelastic deformation at least in one side of the fault. Since it was found that the widest zone of inelastic deformation is diagnosed in the upper section of the footwall, which is also characterized by a higher degree of anisotropy (P), it is quite possible that the main fracture propagation was towards the surface as expected during an earthquake event (Fig. 15).

Marcén et al. (2019) show that the directions of AMS axes in the deformed zone of a large-scale active normal fault system (Baza Fault System) is compatible with the local strain field. They infer that the lithology and distance from secondary fault planes control the development of extension-related magnetic fabrics. The present results show that the magnetic deformation fabrics could be arranged differently around the fault. For example, while some of the K_1 or K_2 axes are sub-parallel to the dip of the fault, the directions of other K_1 or K_2 are varied. Moreover, zones of deposition fabrics are found also close to the fault plane. It is likely that these differences between the two studied areas are mainly related to the deformation settings in which the magnetic fabric developed. In the case of “Baza Fault System” the deformation around the faults is the sum of several seismic and a-seismic slip events that occurred during a long-lasting extensional regime. On

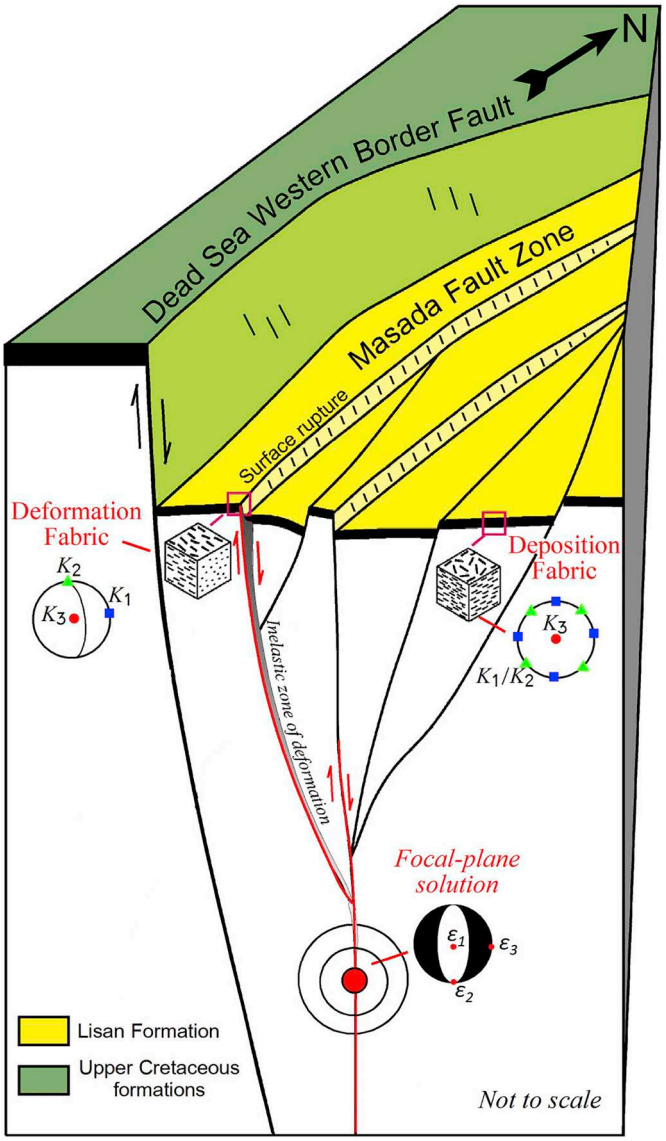

Fig. 15. Schematic cartoon illustrating the Masada Fault Zone and its assumed continuation downwards at the western margin of the Dead Sea Basin. Hypothetical earthquake with a normal mechanism ruptures the surface (i.e., bottom of Lake Lisan), forming inelastic zones of deformation along individual fault strands. The inelastic strain field at the propagating dynamic fault tip may facilitate re-arrangement of particles, obliterating the deposition fabrics and forming deformation fabrics. The studied fault (red lines) formed during a single earthquake event while other faults (black lines) formed in other events. (For interpretation of the references to colour in this figure legend, the reader is referred to the web version of this article.)

the other hand, the studied fault propagated during a single event of seismic slip, forming a "patch-like" pattern of inelastic deformation with varied directions of the AMS axes. Certainly, differences caused by the resolution of spatial sampling should also be considered in the comparison between the two studies.

6.3. Magnetic phases in the Lisan Formation

The similarity of RT-AMS and LT-AMS deformation fabrics (Fig. 11) for the detritus-rich layers suggest that the paramagnetic phase dominates the total magnetic fabric (Kuehn et al., 2019; Marcén et al., 2019) in those layers. The contribution of the diamagnetic phase to mean susceptibility of the detritus-rich specimens is negligible. While the ferromagnetic phase contributes to the mean susceptibility of the detritus-rich specimens (Fig. 10), the AARM shows different fabrics compared to the tectonic RT-AMS and LT-AMS (Fig. 11). In general, the AARM fabrics are different than the RT-AMS fabrics. For example, in Fig. 12d the RT-AMS fabric is deformation, while the AARM fabric is deposition (Fig. 12i). In contrast, in Fig. 12b the RT-AMS fabric is deposition, while the AARM fabric is deformation. This means that the response of the ferromagnetic phase to a certain inelastic strain magnitude could be different than that of the paramagnetic phase (see also Levi et al., 2014; Weinberger et al., 2017).

In the aragonite-rich layers, while the similarity of the RT-AMS and LT-AMS deformation fabrics also implies the dominance of the paramagnetic phase, the contribution of the diamagnetic and ferromagnetic phases must be considered. The predicted $k_{md} + k_{mf}$ (Fig. 10), which is close to the susceptibility value of pure aragonite implies to the importance of the diamagnetic phase. Moreover, higher P values (in average) are observed in the aragonite-rich layers in comparison with the detritus-rich layers, for both deformation and deposition fabrics (Fig. 6b, 6c; See also Levi et al., 2018), suggesting that the aragonite is inherently more magnetically anisotropic than the phyllosilicate. Therefore, in an evolved magnetic fabric acquired during deformation, the magnetic fabric of the diamagnetic phase is expected to be dominant in aragonite-rich layers.

Based on Borradaile and Jackson (2010), if the content of the Fe2+, Fe3+ and Mn2+ ions (i.e., the major sources of paramagnetic minerals) is more than 0.5% (i.e., by mass), the positive susceptibilities of these ions outweigh the diamagnetic susceptibilities of the bulk material. In the aragonite specimens the percentage of Fe and Mn is less than 0.2%, implying also the dominancy of the diamagnetic fabric (Levi et al., 2014). The AARM of the aragonite-rich layers shows a sub-deposition fabric. While similar in magnetic axes directions to the RT-AMS and LT-AMS fabrics, the confidence ellipses are larger (Fig. 11).

We suggest that the high level of the inelastic strain that was developed close to the propagating rupture tip (e.g., Freund, 1998) rotated the paramagnetic clay minerals and the diamagnetic aragonite needles (Fig. 15). In previous works (Alsop et al., 2020; Weinberger et al., 2017), it has been shown that aragonite needles and phyllosilicate plates were aligned the fold hinges in earthquake-triggered slump folds in the Lisan Formation. In the phyllosilicate case it is possible that the clusters of phyllosilicate form an apparent shape, in which the axes of the intersection between the differently oriented basal planes (Cifelli et al., 2004) are parallel to the K_1 axes and to the maximum extension axes (ε_3'). In this case the perpendicular axes to the basal planes are parallel to the K_3 axes and to the maximum shortening axes (ε_1'). In the case of clusters of aragonite, it is likely that the c-axes of the aragonite needles are parallel to the vertical K_3 axes and to the maximum shortening axes (ε_1'), whereas the long axes of the apparent shape is parallel to K_1 axes and to the maximum extension axes (ε_3').

We note that in this study the LT-AMS and phase separation methods were applied for the first time to characterize the magnetic phases of the Lisan Formation. In future work, the complex and varied mineralogy of the Lisan Formation should be further studied. Specifically, in order to better study the contribution of the diamagnetic phase, it is suggested to look for relatively thick (> 2 cm) and seldom observed Lisan layers with negative susceptibility, which consist solely of aragonite. This will help to better elucidate the role played by the aragonite needles to the deformation fabrics by comparing a pure diamagnetic fabric with composite magnetic fabrics in the Lisan Formation. The ferromagnetic phase, which shows both similar and different fabrics compared to the RT-AMS fabrics, should also be further studied.

7. Conclusions

The results show that in the detritus-rich layer the paramagnetic phase is dominant, with some ferromagnetic contribution. In the aragonite-rich layer, the paramagnetic and the diamagnetic phases are

both dominant with possibly some ferromagnetic contribution.

Deformation fabrics detected close to the surface ruptures reveal the inelastic strain that was formed during co-seismic faulting associated with M > 6.5 earthquake events in the Dead Sea Basin, triggered mainly by *E*-W extension as revealed by structural measurements and analysis of fault-plane solutions.

Spatial analyses of the AMS data near a representative co-seismic, single slip fault, shows three main zones of inelastic deformation: Two zones are located asymmetrically at the fault edges, where the displacement values are the lowest, and one zone is located where the displacement values are the highest. Stress perturbations formed during fault propagation along a rough or asperity-rich plane, may be the origin of the "patch-like" distribution of deformation around the fault. Moreover, the fault propagated during a single event, contributing to this discontinuous deformation. The main propagation of the fault was towards the surface, as indicated by: (1) the widest zone of inelastic deformation which was diagnosed in the upper section of the footwall and characterized by high degree of anisotropy (*P*) values, and (2) many of the AMS principal directions are compatible with the fault-plane solution in this area.

This study demonstrates that AMS analyses can be used for detecting zones of inelastic deformation around faults and surface ruptures, namely by studying the spatial distribution of AMS data, which could be useful for characterizing the individual earthquakes that ruptured the host rock.

Declaration of Competing Interest

The authors declare that they have no known competing financial interests or personal relationships that could have appeared to influence the work reported in this paper.

Acknowledgments

This study was supported by grants from the Israel Science Foundation (ISF grant No. 868/17) and the Israeli Government (under the Geological Survey of Israel, Dead Sea, project 40706). SM was supported by the Israel Science Foundation (ISF grant No. 1645/19). We thank Ran Issachar for field assistance and helpful discussions during the course of this study, and Alon Ziv and Meir Abelson for insightful comments. We are grateful to Ruth Soto and an anonymous reviewer for providing constructive and very helpful reviews.

Appendix A. Supplementary data

Supplementary data to this article can be found online at https://doi.org/10.1016/j.tecto.2020.228502.

References

Agnon, A., Migowski, C., Marco, S., 2006. Intraclast breccias in laminated sequences reviewed: Recorders of paleo-earthquakes. Spec. Pap. Geol. Soc. Am. 195–214 doi:10.1130/2006.2401(13).

Allmendinger, R.W., Cardozo, N., Fisher, D.M., 2011. Structural geology algorithms: Vectors and tensors. In: Structural Geology Algorithms: Vectors and Tensors, https://doi.org/10.1017/CBO9780511920202.

Alsop, G.I., Marco, S., Levi, T., Weinberger, R., 2017. Fold and thrust systems in mass transport deposits. J. Struct. Geol. 94, 98–115. https://doi.org/10.1016/j.jsg.2016.11.008.

Alsop, G.I., Weinberger, R., Marco, S., Levi, T., 2020. Distinguishing coeval patterns of contraction and collapse around flow lobes in mass transport deposits. J. Struct. Geol. https://doi.org/10.1016/j.jsg.2020.104013.

Beck, C., 2009. Late Quaternary lacustrine paleo-seismic archives in North-Western Alps: examples of earthquake-origin assessment of sedimentary disturbances. Earth-Sci. Rev. 96, 327–344. https://doi.org/10.1016/j.earscirev.2009.07.005.

Begin, Z.B., Ehrlich, A., Nathan, Y., 1974. Lake Lisan – the Pleistocene precursor of the Dead Sea. Geol. Surv. Isr. Bull. 30.

Begin, Z.B., Steinberg, D.M., Ichinose, G.A., Marco, S., 2005. A 40,000 year unchanging seismic regime in the Dead Sea rift. Geology 33, 257–260. https://doi.org/10.1130/G21115.1.

Ben-Menahem, A., Nur, A., Vered, M., 1976. Tectonics, seismicity and structure of the Afro-Eurasian junction - the breaking of an incoherent plate. Phys. Earth Planet. Inter. https://doi.org/10.1016/0031-9201(76)90005-4.

Ben-Zion, Y., Shi, Z., 2005. Dynamic rupture on a material interface with spontaneous generation of plastic strain in the bulk. Earth Planet. Sci. Lett. 236, 486–496. https://doi.org/10.1016/j.epsl.2005.03.025.

Borradaile, G.J., 1987. Anisotropy of magnetic susceptibility: rock composition versus strain. Tectonophysics 138, 327–329. https://doi.org/10.1016/0040-1951(87)90051-5.

Borradaile, G.J., 1988. Magnetic-susceptibility, petrofabrics and strain. Tectonophysics 156, 1–20. https://doi.org/10.1016/0040-1951(88)90279-x.

Borradaile, G.J., 1991. Correlation of strain with anisotropy of magnetic susceptibility (AMS). Pure Appl. Geophys. 135, 15–29. https://doi.org/10.1007/bf00877006.

Borradaile, G.J., Henry, B., 1997. Tectonic applications of magnetic susceptibility and its anisotropy. Earth-Sci. Rev. 42, 49–93. https://doi.org/10.1016/S0012-8252(96)00044-X.

Borradaile, G.J., Jackson, M., 2004. Anisotropy of magnetic susceptibility (AMS): magnetic petrofabrics of deformed rocks. Geol. Soc. London, Spec. Publ. 238, 299–360. https://doi.org/10.1144/GSL.SP.2004.238.01.18.

Borradaile, G.J., Jackson, M., 2010. Structural geology, petrofabrics and magnetic fabrics (AMS, AARM, AIRM). J. Struct. Geol. 32, 1519–1551. https://doi.org/10.1016/j.jsg.2009.09.006.

Braun, D., Weinberger, R., Eyal, Y., Feinstein, S., Harlavan, Y., Levi, T., 2015. Distinctive diamagnetic fabrics in dolostones evolved at fault cores, the Dead Sea Transform. J. Struct. Geol. 77, 11–26. https://doi.org/10.1016/j.jsg.2015.05.007.

Butler, R.F., 1998. Chapter 2 - Ferromagnetic minerals. In: Paleomagnetism: Magnetic Domains to Geologic Terranes, pp. 16–30.

Cardozo, N., Allmendinger, R.W., 2013. Spherical projections with OSXStereonet. Comput. Geosci. https://doi.org/10.1016/j.cageo.2012.07.021.

Casas-Sainz, A.M., Gil-Imaz, A., Simón, J.L., Izquierdo-Llavall, E., Aldega, L., Román-Berdiel, T., Osácar, M.C., Pueyo-Anchuela Ansón, M., García-Lasanta, C., Corrado, S., Invernizzi, C., Caricchi, C., 2018. Strain indicators and magnetic fabric in intraplate fault zones: Case study of Daroca thrust, Iberian Chain, Spain. Tectonophysics 730, 29–47. https://doi.org/10.1016/j.tecto.2018.02.013.

Cifelli, F., Mattei, M., Hirt, A.M., Günther, A., 2004. The origin of tectonic fabrics in "undeformed" clays: the early stages of deformation in extensional sedimentary basins. Geophys. Res. Lett. 31, 2–5. https://doi.org/10.1029/2004GL019609.

Cifelli, F., Mattei, M., Chadima, M., Hirt, A.M., Hansen, A., 2005. The origin of tectonic lineation in extensional basins: combined neutron texture and magnetic analyses on "undeformed" clays. Earth Planet. Sci. Lett. 235, 62–78. https://doi.org/10.1016/j.epsl.2005.02.042.

Enzel, Y., Kadan, G., Eyal, Y., 2000. Holocene earthquakes inferred from a fan-delta sequence in the Dead Sea graben. Quat. Res. 53, 34–48. https://doi.org/10.1006/qres.1999.2096.

Eyal, Y., Bruner, I., Cadan, G., Enzel, Y., Landa, E., 2002. High-resolution seismic study of the Nahal Darga fan-delta, Dead Sea, Israel, with the aim to relate the surface and subsurface tectonic structures. Stephan Mueller Spec. Publ. Ser. https://doi.org/10.5194/smsps-2-21-2002.

Faulkner, D.R., Jackson, C.A.L., Lunn, R.J., Schlische, R.W., Shipton, Z.K., Wibberley, C.A.J., Withjack, M.O., 2010. A review of recent developments concerning the structure, mechanics and fluid flow properties of fault zones. J. Struct. Geol. 32, 1557–1575. https://doi.org/10.1016/j.jsg.2010.06.009.

Faulkner, D.R., Mitchell, T.M., Jensen, E., Cembrano, J., 2011. Scaling of fault damage zones with displacement and the implications for fault growth processes. J. Geophys. Res. Solid Earth 116, 1–11. https://doi.org/10.1029/2010JB007788.

Freund, L.B., 1998. Dynamic Fracture Mechanics. Cambridge university press.

Fusseis, F., Xiao, X., Schrank, C., De Carlo, F., 2014. A brief guide to synchrotron radiation-based microtomography in (structural) geology and rock mechanics. J. Struct. Geol. 65, 1–16. https://doi.org/10.1016/j.jsg.2014.02.005.

García-Lasanta, C., Oliva-Urcia, B., Román-Berdiel, T., Casas, A.M., Perez-Lorente, F., 2013. Development of magnetic fabric in sedimentary rocks: Insights from early compactional structures. Geophys. J. Int. 194, 182–199. https://doi.org/10.1093/gji/ggt098.

Garfunkel, Z., Zak, I., Freund, R., 1981. Active faulting in the dead sea rift. Tectonophysics 80, 1–26.

Haase-Schramm, A., Goldstein, S.L., Stein, M., 2004. U-Th dating of Lake Lisan (late Pleistocene dead sea) aragonite and implications for glacial East Mediterranean climate change. Geochim. Cosmochim. Acta. https://doi.org/10.1016/j.gca.2003.07.016.

Hirt, A.M., Julivert, M., Soldevila, J., 2000. Magnetic fabric and deformation in the Navia-Alto Sil slate belt, northwestern Spain. Tectonophysics 320, 1–16. https://doi.org/10.1016/S0040-1951(00)00047-0.

Hrouda, F., 1982. Magnetic anisotropy of rocks and its application in geology and geophysics. Geophys. Surv. 5, 37–82. https://doi.org/10.1007/BF01450244.

Hrouda, F., 1993. Theoretical models of magnetic anisotropy to strain relationship revisited. Phys. Earth Planet. Inter. 77, 237–249. https://doi.org/10.1016/0031-9201(93)90101-E.

Hrouda, F., 1994. A technique for the measurement of thermal changes of magnetic susceptibility of weakly magnetic rocks by the CS-2 apparatus and KLY-2 Kappabridge. Geophys. J. Int. 118, 604–612. https://doi.org/10.1111/j.1365-246X.1994.tb03987.x.

Issachar, R., Levi, T., Marco, S., Weinberger, R., 2015. Anisotropy of magnetic susceptibility in diamagnetic limestones reveals deflection of the strain field near the Dead Sea Fault, northern Israel. Tectonophysics 656, 175–189. https://doi.org/10.1016/j.tecto.2015.06.021.

Issachar, R., Levi, T., Lyakhovsky, V., Marco, S., Weinberger, R., 2016. Improving the

method of low-temperature anisotropy of magnetic susceptibility (LT-AMS) measurements in air. Geochemistry, Geophys. Geosystems 2940–2950 doi:10.1002/2016GC006339.Received.
Issachar, R., Levi, T., Marco, S., Weinberger, R., 2018. Separation of Diamagnetic and Paramagnetic Fabrics reveals Strain Directions in Carbonate Rocks. J. Geophys. Res. Solid Earth 123, 2035–2048. https://doi.org/10.1002/2017JB014823.
Jacoby, Y., Weinberger, R., Levi, T., Marco, S., 2015. Clastic dikes in the Dead Sea basin as indicators of local site amplification. Nat. Hazards 75, 1649–1676. https://doi.org/10.1007/s11069-014-1392-0.
Jelínek, V., 1981. Characterization of the magnetic fabric of rocks. Tectonophysics 79, 63–67. https://doi.org/10.1016/0040-1951(81)90110-4.
Ken-Tor, R., Agnon, A., Yehouda, E., Stein, M., Marco, S., Negendank, J.F.W., 2001. High-resolution geological record of historic earthquakes in the Dead Sea basin. Geophys. Res. 106, 2221–2234.
Kim, Y.S., Sanderson, D.J., 2005. The relationship between displacement and length of faults: a review. Earth-Sci. Rev. 68, 317–334. https://doi.org/10.1016/j.earscirev.2004.06.003.
Kuehn, R., Hirt, A.M., Biedermann, A.R., Leiss, B., 2019. Quantitative comparison of microfabric and magnetic fabric in black shales from the Appalachian plateau (western Pennsylvania, U.S.A.). Tectonophysics 765, 161–171. https://doi.org/10.1016/j.tecto.2019.04.013.
Levi, T., Weinberger, R., 2011. Magnetic fabrics of diamagnetic rocks and the strain field associated with the Dead Sea Fault, northern Israel. J. Struct. Geol. 33, 566–578. https://doi.org/10.1016/j.jsg.2011.02.001.
Levi, T., Weinberger, R., Aïfa, T., Eyal, Y., Marco, S., 2006a. Injection mechanism of clay-rich sediments into dikes during earthquakes. Geochemistry, Geophys. Geosystems 7. https://doi.org/10.1029/2006GC001410.
Levi, T., Weinberger, R., Aïfa, T., Eyal, Y., Marco, S., 2006b. Earthquake-induced clastic dikes detected by anisotropy of magnetic susceptibility. Geology 34, 69–72. https://doi.org/10.1130/G22001.1.
Levi, T., Weinberger, R., Eyal, Y., 2011. A coupled fluid-fracture approach to propagation of clastic dikes during earthquakes. Tectonophysics 498, 35–44. https://doi.org/10.1016/j.tecto.2010.11.012.
Levi, T., Weinberger, R., Marco, S., 2014. Magnetic fabrics induced by dynamic faulting reveal damage zone sizes in soft rocks, Dead Sea basin. Geophys. J. Int. Geophys. J. Int 199, 1214–1229. https://doi.org/10.1093/gji/ggu300.
Levi, T., Weinberger, R., Alsop, G.I., Marco, S., 2018. Characterizing seismites with anisotropy of magnetic susceptibility. Geology 46, 827–830. https://doi.org/10.1130/G45120.1.
Levi, T., Avni, Y., Bahat, D., 2019. Evolution of the stress field near the Arava basin located along the Dead Sea Fault system as revealed by joint sets. J. Struct. Geol. https://doi.org/10.1016/j.jsg.2019.103876.
Li, B., Tan, X., Wang, F., Lian, P., Gao, W., Li, Y.G., 2017. Fracture and vug characterization and carbonate rock type automatic classification using X-ray CT images. J. Pet. Sci. Eng. 153, 88–96. https://doi.org/10.1016/j.petrol.2017.03.037.
Ma, S., Andrews, D.J., 2010. Inelastic off - fault response and three - dimensional dynamics of earthquake rupture on a strike - slip fault. J. Geophys. Res. 115, 1–16. https://doi.org/10.1029/2009JB006382.
Madhur, J., Dunham, E.M., Zoback, M.D., Zijun, F., 2014. Predicting fault damage zones by modeling dynamic rupture propagation and comparison with field observations. J. Geophys. Res. Solid Earth 1251–1272. https://doi.org/10.1002/2013JB010335.Received.
Mamtani, M.A., Sengupta, A., 2009. Anisotropy of magnetic susceptibility analysis of deformed kaolinite: Implications for evaluating landslides. Int. J. Earth Sci. 98, 1721–1725. https://doi.org/10.1007/s00531-008-0336-x.
Marcén, M., Román-Berdiel, T., Casas-Sainz, A.M., Soto, R., Oliva-Urcia, B., Castro, J., 2019. Strain variations in a seismogenic normal fault (Baza Sub-basin, Betic Chain): Insights from magnetic fabrics (AMS). Tectonophysics 765, 64–82. https://doi.org/10.1016/j.tecto.2019.05.014.
Marco, S., Agnon, A., 1995. Prehistoric earthquake deformations near Masada, Dead Sea graben. Geology 23, 695–698. https://doi.org/10.1130/0091-7613(1995)023<0695:PEDNMD>2.3.CO;2.
Marco, S., Agnon, A., 2005. High-resolution stratigraphy reveals repeated earthquake faulting in the Masada Fault Zone, Dead Sea Transform. Tectonophysics 408, 101–112. https://doi.org/10.1016/j.tecto.2005.05.036.
Marco, S., Stein, M., Agnon, A., 1996. Long-term earthquake clustering: a 50,000-year paleoseismic record in the Dead Sea Graben. J. Geophys. Res. 101, 6179–6191. https://doi.org/10.1029/95JB01587.
Marco, S., Ron, H., McWilliams, M.O., Stein, M., 1998. High-resolution record of geomagnetic secular variation from late Pleistocene Lake Lisan sediments (paleo Dead Sea). Earth Planet. Sci. Lett. 161, 145–160. https://doi.org/10.1016/S0012-821X(98)00146-0.
Marrett, R., Allmendinger, R.W., 1990. Kinematic analysis of fault-slip data. J. Struct. Geol. https://doi.org/10.1016/0191-8141(90)90093-E.
Martínez-Martínez, J., Fusi, N., Galiana-Merino, J.J., Benavente, D., Crosta, G.B., 2016. Ultrasonic and X-ray computed tomography characterization of progressive fracture damage in low-porous carbonate rocks. Eng. Geol. 200, 47–57. https://doi.org/10.1016/j.enggeo.2015.11.009.
Mattei, M., Sagnotti, L., Faccenna, C., Funiciello, R., 1997. Magnetic fabric of weakly deformed clay-rich sediments in the Italian peninsula: Relationship with compressional and extensional tectonics. Tectonophysics 271, 107–122.
Mattei, M., Speranza, F., Argentieri, A., Rossetti, F., Sagnotti, L., Funiciello, R., 1999. Extensional tectonics in the Amatea basin (Calabria, Italy) : a comparison between structural and magnetic anisotropy data. Tectonophysics 307, 33–49.
Morin, F.J., 1950. Magnetic susceptibility of αFe2O3 and αFe2O3 with added titanium. Phys. Rev. 78, 819–820. https://doi.org/10.1103/PhysRev.78.819.2.
Muraoka, H., Kamata, H., 1983. Displacement distribution along minor fault traces. J. Struct. Geol. 5, 483–495. https://doi.org/10.1016/0191-8141(83)90054-8.
Oliva-Urcia, B., Román-Berdiel, T., Casas, A.M., Bogalo, M.F., Osácar, M.C., García-Lasanta, C., 2013. Transition from extensional to compressional magnetic fabrics in the cretaceous Cabuérniga basin (North Spain). J. Struct. Geol. 46, 220–234. https://doi.org/10.1016/j.jsg.2012.09.001.
Pares, J.P., Van Der Pluijm, B.A., Dinarès-Turell, J., 1999. Evolution of magnetic fabric during incipient deformation of mudrock (Pyrenees, northen Spain). Tectonophysics 307, 1–14.
Rees, A.I., 1971. The magnetic fabric of a sedimentary rock deposited on a slope. J. Sediment. Res. 41, 307–309. https://doi.org/10.1306/74d72257-2b21-11d7-8648000102c1865d.
Rees, A.I., Woodall, W.A., 1975. The magnetic fabric of some laboratory-deposited sediments. Earth Planet. Sci. Lett. https://doi.org/10.1016/0012-821X(75)90188-0.
Rice, J.R., Sammis, C.G., Parsons, R., 2005. Off-fault secondary failure induced by a dynamic slip pulse. Bull. Seismol. Soc. Am. 95, 109–134. https://doi.org/10.1785/0120030166.
Ron, H., Nowaczyk, N.R., Frank, U., Marco, S., McWilliams, M.O., 2006. Magnetic properties of Lake Lisan and Holocene Dead Sea sediments and the fidelity of chemical and detrital remanent magnetization. New Front. Dead Sea Paleoenviron. Res. 80301 (11), 171–182. https://doi.org/10.1130/2006.2401.
Sagy, A., Reches, Z., Agnon, A., 2003. Hierarchic three-dimensional structure and slip partitioning in the western Dead Sea pull-apart. Tectonics 22, 1–17. https://doi.org/10.1029/2001TC001323.
Shapira, A., Avni, R., Nur, A., 1993. A new estimate for the epicenter of the Jericho earthquake of 11 July 1927. Isr. J. Earth Sci. 42, 93–96.
Shearer, P.M., 2009. Introduction to Seismology. Cambridge university presshttps://doi.org/10.1111/j.1365-246X.1975.tb01612.x.
Sneh, A., Weinberger, R., 2014. Major Structures of Israel and Environs, Scale 1:500,000: Jerusalem, Israel Geological Survey.
Sneh, A., Bartov, Y., Weissbrod, T., Rosensaft, M., 1998. Geological Map of Israel. (scale 1:500,000: Jerusalem, Israel Geological Survey).
Soto, R., Casas-Sainz, A.M., Villalaín, J.J., Oliva-Urcia, B., 2007. Mesozoic extension in the Basque-Cantabrian basin (N Spain): Contributions from AMS and brittle mesostructures. Tectonophysics 445, 373–394. https://doi.org/10.1016/j.tecto.2007.09.007.
Soto, R., Larrasoaña, J.C., Arlegui, L.E., Beamud, E., Oliva-Urcia, B., Simón, J.L., 2009. Reliability of magnetic fabric of weakly deformed mudrocks as a palaeostress indicator in compressive settings. J. Struct. Geol. 31, 512–522. https://doi.org/10.1016/j.jsg.2009.03.006.
Soto, R., Beamud, E., Oliva-Urcia, B., Roca, E., Rubinat, M., Villalaín, J.J., 2014. Applicability of magnetic fabrics in rocks associated with the emplacement of salt structures (the Bicorb-Quesa and Navarrés salt walls, Prebetics, SE Spain). Tectonophysics. https://doi.org/10.1016/j.tecto.2014.07.004.
Taira, A., 1989. Magnetic fabrics and depositional processes. Sedimentary facies in the active plate margin 43–47.
Tarling, D.H., Hrouda, F., 1993a. Magnetic Anisotropy of Rocks. https://doi.org/10.1016/0040-1951(94)90154-6.
Tarling, D.H., Hrouda, F., 1993b. The Magnetic Anisotropy of Rocks. Chapman & Hallhttps://doi.org/10.1002/gj.3350300111.
Verwey, E.J.W., 1939. Electronic conduction of magnetite (Fe3O4) and its transition point at low temperatures. Nature 144, 327–328.
Weinberger, R., Levi, T., Alsop, G.I., Eyal, Y., 2016. Coseismic horizontal slip revealed by sheared clastic dikes in the Dead Sea Basin. Bull. Geol. Soc. Am. 128, 1193–1206. https://doi.org/10.1130/B31415.1.
Weinberger, R., Levi, T., Alsop, G.I., Marco, S., 2017. Kinematics of Mass Transport Deposits revealed by magnetic fabrics. Geophys. Res. Lett. 5807–5817. https://doi.org/10.1002/2017GL072584.
Wells, D.L., Coppersmith, K.J., 1994. New empical relationship between magnitude, rupture length, rupture width, rupture area, and surface displacement. Bull. Seismol. Soc. Am. 84.